# Unveiling the internal structure and formation history of the three planets transiting HIP 29442 (TOI-469) with CHEOPS

(article starts on next page)

**Astronomy & Astrophysics**

# Unveiling the internal structure and formation history of the three planets transiting HIP 29442 (TOI-469) with CHEOPS⋆

J. A. Egger [1], H. P. Osborn [2,3], D. Kubyshkina [4], C. Mordasini [1,2], Y. Alibert [2,1], M. N. Günther [5], M. Lendl [6],
A. Brandeker [7], A. Heitzmann [6], A. Leleu [6,1], M. Damasso [8], A. Bonfanti [4], T. G. Wilson [9], S. G. Sousa [10],
J. Haldemann [1], L. Delrez [11,12,13], M. J. Hooton [14], T. Zingales [15,16], R. Luque [17], R. Alonso [18,19], J. Asquier [5],
T. Bárczy [20], D. Barrado Navascues [21], S. C. C. Barros [10,22], W. Baumjohann [4], W. Benz [1,2], N. Billot [6],
L. Borsato [16], C. Broeg [1,2], M. Buder [23], A. Castro-González [21], A. Collier Cameron [24], A. C. M. Correia [25],
D. Cortes [26], Sz. Csizmadia [27], P. E. Cubillos [28,4], M. B. Davies [29], M. Deleuil [30], A. Deline [6],
O. D. S. Demangeon [10,22], B.-O. Demory [2,1], A. Derekas [31], B. Edwards [32], D. Ehrenreich [6,33], A. Erikson [27],
A. Fortier [1,2], L. Fossati [4], M. Fridlund [34,35], D. Gandolfi [36], K. Gazeas [37], M. Gillon [11], M. Güdel [38],
Ch. Helling [4,39], K. G. Isaak [5], L. L. Kiss [40,41], J. Korth [42], K. W. F. Lam [27], J. Laskar [43], B. Lavie [6],
A. Lecavelier des Etangs [44], C. Lovis [6], A. Luntzer [38], D. Magrin [16], P. F. L. Maxted [45], B. Merín [46], M. Munari [47],
V. Nascimbeni [16], G. Olofsson [7], R. Ottensamer [38], I. Pagano [47], E. Pallé [18,19], G. Peter [23], D. Piazza [1],
G. Piotto [16,15], D. Pollacco [9], D. Queloz [48,14], R. Ragazzoni [16,15], N. Rando [5], H. Rauer [27,49], I. Ribas [50,51],
J. Rodrigues [52,53], N. C. Santos [10,22], G. Scandariato [47], D. Ségransan [6], A. E. Simon [1,2], A. M. S. Smith [27],
M. Stalport [12,11], S. Sulis [30], Gy. M. Szabó [31,54], S. Udry [6], V. Van Grootel [12], J. Venturini [6],
E. Villaver [18,19], and N. A. Walton [55]

*(Affiliations can be found after the references)*

## ABSTRACT

Multiplanetary systems spanning the radius valley are ideal testing grounds for exploring the different proposed explanations for the observed bimodality in the radius distribution of close-in exoplanets. One such system is HIP 29442 (TOI-469), an evolved K0V star hosting two super-Earths and one sub-Neptune. We observed HIP 29442 with CHEOPS for a total of 9.6 days, which we modelled jointly with two sectors of TESS data to derive planetary radii of $3.410 \pm 0.046$, $1.551 \pm 0.045$, and $1.538 \pm 0.049$ $R_\oplus$ for planets b, c, and d, which orbit HIP 29442 with periods of 13.6, 3.5, and 6.4 days, respectively. For planet d this value deviates by more than $3\sigma$ from the median value reported in the discovery paper, leading us to conclude that caution is required when using TESS photometry to determine the radii of small planets with low per-transit signal-to-noise ratios and large gaps between observations. Given the high precision of these new radii, combining them with published RVs from ESPRESSO and HIRES provides us with ideal conditions to investigate the internal structure and formation pathways of the planets in the system. We introduced the publicly available code `plaNETic`, a fast and robust neural network-based Bayesian internal structure modelling framework. We then applied hydrodynamic models to explore the upper atmospheric properties of these inferred structures. Finally, we identified planetary system analogues in a synthetic population generated with the Bern model for planet formation and evolution. Based on this analysis, we find that the planets likely formed on opposing sides of the water iceline from a protoplanetary disk with an intermediate solid mass. We finally report that the observed parameters of the HIP 29442 system are compatible with a scenario where the second peak in the bimodal radius distribution corresponds to sub-Neptunes with a pure H/He envelope and with a scenario with water-rich sub-Neptunes.

**Key words.** techniques: photometric – planets and satellites: formation – planets and satellites: interiors – planets and satellites: individual: HIP 29442 – planetary systems

## 1. Introduction

One of the most notable features in the observed exoplanet population is the radius valley, an underdensity of small exoplanets with radii between ∼1.5 and ∼2 $R_\oplus$ at orbital periods of less than 100 days. This bimodality in the radius distribution with two distinct peaks at ∼1.3 and ∼2.4 $R_\oplus$, with the planets corresponding to the two peaks commonly referred to as super-Earths and sub-Neptunes, was first observationally confirmed by the California-Kepler Survey (Fulton et al. 2017), after a photoevaporation valley had already been predicted theoretically by several groups (e.g. Owen & Wu 2013; Jin et al. 2014; Lopez & Fortney 2014).

The origin of the radius valley is still heavily debated in the literature, and multiple possible explanations have been brought forward. On the one hand, it has been proposed that the observed gap in the radius distribution is caused by planets being stripped of their H/He envelopes through an atmospheric mass loss mechanism and remaining as bare rocky cores, with photoevaporation via high-energy stellar irradiation (Owen & Wu 2017;

Jin & Mordasini 2018) and core-powered mass loss (Ginzburg et al. 2018; Gupta & Schlichting 2019) as the most commonly presented scenarios. On the other hand, planet formation predicts water-rich planets to migrate inwards from beyond the iceline (e.g. Tanaka et al. 2002), which is inconsistent with a picture where the majority of sub-Neptunes are water-poor and feature pure H/He envelopes. It has therefore been proposed that the second peak of the observed radius distribution is instead populated by planets that are mostly water-rich.

While this hypothesis was first presented based on mass–radius curves for water-rich planets (Sotin et al. 2007; Valencia et al. 2013; Zeng et al. 2019; Turbet et al. 2020; Mousis et al. 2020), Venturini et al. (2020a,b) then showed for the first time that the observed location of the radius valley can be reproduced using pebble-based combined formation and evolution models when treating water in vapour form uniformly mixed with H/He; their newer work expands this for M-dwarf stars (Venturini et al. 2024). Izidoro et al. (2022) reach similar conclusions for planets with water in condensed form, but also including the gravitational interaction between planets. More recently, Burn et al. (2024) have been able to naturally reproduce the observed location of the radius valley using a planetesimal-based combined planet formation and evolution model and again assuming water to be in gaseous form mixed with H/He, supporting the scenario of water-rich sub-Neptunes with supercritical steam atmospheres.

Distinguishing between these different scenarios observationally is challenging, as the information we have about these planets is generally very limited. Even if both the mass and radius of a given planet are known in addition to its orbital period, determining the internal structure and composition of the planet is still a highly degenerate problem (e.g. Seager et al. 2007; Rogers & Seager 2010). A wide variety of internal structure modelling approaches can be found in the literature (e.g. Brugger et al. 2017; Dorn et al. 2017; Baumeister et al. 2020; Acuña et al. 2021; Vazan et al. 2022; Unterborn et al. 2023; Haldemann et al. 2023, 2024), many of them coupling the internal structure model with Bayesian inference or machine learning approaches in order to determine a probability distribution for the interior composition of an exoplanet. However, these methods only allow us to quantify the degenerate nature of the problem, while the actual degeneracy cannot be broken without additional observational data, such as spectroscopic observations of the planet's atmosphere. Observational evidence for water-rich sub-Neptunes has been presented by Luque & Pallé (2022) for planets around M dwarfs, who show that many planets in their sample are consistent with a 1:1 water-to-rock ratio. However, Rogers et al. (2023) point out that these observations can also be explained by planets with H/He dominated atmospheres. Furthermore, recent analyses of JWST transmission spectra of sub-Neptunes find high atmospheric metallicities (Benneke et al. 2024; Holmberg & Madhusudhan 2024; Madhusudhan et al. 2023).

When studying the different explanations for the radius valley, multiplanetary systems with planets on either side of the radius valley provide us with an ideal testing ground for the different hypotheses as they were formed from the same protoplanetary disk and orbit the same star. Currently, there are only a few such systems with well-characterised masses and radii. A search of the NASA Exoplanet Archive[1] revealed 16 radius valley crossing systems with mass errors smaller than 25% and radius errors smaller than 10%. Of these, only six systems have

mass errors smaller than 15% and radius errors smaller than 5% ($\nu^2$ Lupi, Delrez et al. 2021; Ehrenreich et al. 2023; Kepler-10, Batalha et al. 2011; Fressin et al. 2011; Bonomo et al. 2023; Kepler-36, Carter et al. 2012; Vissapragada et al. 2020; LTT 3780, Cloutier et al. 2020; Bonfanti et al. 2024; TOI-1468, Chaturvedi et al. 2022; TOI-561, Lacedelli et al. 2022; Patel et al. 2023). Of particular interest is the TOI-178 system (Leleu et al. 2021; Delrez et al. 2023) with six known transiting planets; two super-Earths and four sub-Neptunes. Multiple studies have investigated the internal structure of the planets in this system (Leleu et al. 2021; Acuña et al. 2022), and some of its planets have recently been observed with JWST (Hooton et al. 2021).

Another multiplanetary system with planets on both sides of the radius valley is HIP 29442 (TOI-469), which consists of three known transiting planets (two super-Earths and an outer sub-Neptune) orbiting an evolved K0-type star on short orbits. The outer sub-Neptune, HIP 29442 b, was first identified as a planetary candidate (TOI-469.01) in data from the Transiting Exoplanet Survey Satellite (TESS; Ricker et al. 2015) and later validated by Giacalone et al. (2021), while the two inner super-Earths, HIP 29442 c and d, were discovered using data from the Echelle SPectrograph for Rocky Exoplanets and Stable Spectroscopic Observations (ESPRESSO; Pepe et al. 2021), as presented by Damasso et al. (2023), who then searched for and found the corresponding transits in the TESS light curves. However, as already pointed out by Damasso et al. (2023), these additional transits are extremely shallow, which complicates an accurate determination of the radii for these two planets.

Here, we present the results of an extensive photometric follow-up campaign of HIP 29442 using the CHaracterising ExOPlanet Satellite (CHEOPS; Benz et al. 2021; Fortier et al. 2024), driven by the discovery of the additional shallow transits for HIP 29442 c and d in the TESS data. After newly determining values for the host star radius, mass, and age in Section 2, we present the collected CHEOPS light curves, analyse all available data for this system, and summarise our derived planetary parameters in Section 3. In this section, we also make a comparison with the values of Damasso et al. (2023) and discuss how HIP 29442 b, c, and d fit into the larger exoplanet population given our newly determined radius and mass values for all three planets.

In the subsequent sections, we analyse how the HIP 29442 system fits in with the individual scenarios brought forward to explain the bimodality of the observed radius distribution. In order to do that, we present our improved neural network-based Bayesian internal structure modelling framework `plaNETic` in Section 4 and apply it to the HIP 29442 planets. In Section 5 we employ the 1D hydrodynamic model CHAIN (Kubyshkina et al. 2024) to study the properties of the upper atmosphere and the atmospheric mass loss for the atmospheric compositions inferred in the previous section. Section 6 then discusses possible formation and evolution pathways of the HIP 29442 system by identifying planetary system analogues in a variation of the nominal population of the New Generation Planetary Population Synthesis (Emsenhuber et al. 2021a,b, 2023; Burn et al. 2024) and analysing the common properties of these synthetic systems. We discuss the outcome and limitations of these different analyses in Section 7, before finally drawing conclusions and summarising our findings in Section 8.

## 2. Host star characterisation

For the spectroscopic stellar parameters of HIP 29442, we used the values derived by Damasso et al. (2023). Their values for

---

[1] https://exoplanetarchive.ipac.caltech.edu/, query from 5 June 2024.

**Table 1.** Stellar properties of HIP 29442.

| Star names | | |
| --- | --- | --- |
| HIP | 29442 | |
| HD | 42813 | |
| TOI | 469 | |
| TIC | 33692729 | |
| TYC | 5374-00643-1 | |
| *Gaia* DR3 | 2993561629444856960 | |
| Parameter | Value | Source |
| $\alpha$ (J2000) | 06h12m13.97s | [1] |
| $\delta$ (J2000) | −14°39′00.06′′ | [1] |
| G mag | $9.282 \pm 0.003$ | [1] |
| $T_{\rm eff}$ (K) | $5289 \pm 69$ | [2] |
| $\log g$ (cgs) | $4.39 \pm 0.03$ | [2] |
| [Fe/H] (dex) | $0.24 \pm 0.05$ | [2] |
| [Mg/H] (dex) | $0.26 \pm 0.04$ | [2] |
| [Si/H] (dex) | $0.21 \pm 0.04$ | [2] |
| $R_\star$ ($R_\odot$) | $0.980 \pm 0.007$ | [3] |
| $M_\star$ ($M_\odot$) | $0.901 \pm 0.043$ | [3] |
| $t_\star$ (Gyr) | $11.2 \pm 3.4$ | [3] |

**References.** [1] Gaia Collaboration (2021); [2] Damasso et al. (2023); [3] This work.

the effective temperature, surface gravity and stellar abundances ([Fe/H], [Mg/H] and [Si/H]) are summarised in Table 1. They were consistent with our own additional analysis using the spectral analysis package Spectroscopy Made Easy (SME; Valenti & Piskunov 1996; Piskunov & Valenti 2017).

We then utilised a MCMC modified infrared flux method (Blackwell & Shallis 1977; Schanche et al. 2020) to determine the stellar radius of HIP 29442. The stellar spectral parameters and $1\sigma$ uncertainties from Damasso et al. (2023) were used as priors in constructing spectral energy distributions (SEDs) using stellar atmospheric models from two catalogues (Kurucz 1993; Castelli & Kurucz 2003). Synthetic photometry was computed from these SEDs and compared to the observed broadband photometry in the following bandpasses: *Gaia G*, $G_{\rm BP}$, and $G_{\rm RP}$, 2MASS *J*, *H*, and *K*, and *WISE W*1 and *W*2 (Skrutskie et al. 2006; Wright et al. 2010; Gaia Collaboration 2023) to derive the stellar bolometric flux. We used the Stefan-Boltzmann law to convert the bolometric flux to stellar effective temperature and angular diameter. Using the offset-corrected *Gaia* parallax (Lindegren et al. 2021), we then converted the angular diameter into stellar radius. This process was conducted for both atmospheric catalogues with the produced radius posterior distributions combined via a Bayesian modelling averaging in order to correct for atmospheric model uncertainties. Our weighted average radius value $R_\star$ is reported in Table 1.

We further determined the isochronal mass $M_\star$ and age $t_\star$ of HIP 29442 by inputting $T_{\rm eff}$, [Fe/H], and $R_\star$ along with their uncertainties in the isochrone placement routine by Bonfanti et al. (2015, 2016). In short, the algorithm computes $M_\star$ and $t_\star$ following interpolation of the input parameters within pre-computed grids of PARSEC[2] v1.2S (Marigo et al. 2017) isochrones and evolutionary tracks. As justified in Bonfanti et al. (2021), we inflated the internal uncertainties on mass and age by 4% and 20%, respectively, to account for isochrone

systematics and we obtained $M_\star = 0.901 \pm 0.043$ $M_\odot$ and $t_\star = 11.2 \pm 3.4$ Gyr.

## 3. Observations and data analysis

### 3.1. Photometry

TESS observed HIP 29442 in two sectors, once in December 2018 (Sector 6) and once in December 2020 (Sector 33), at a two-minute cadence on camera 2. In addition, HIP 29442 was then observed by CHEOPS (program CH_PR100031) as part of the Guaranteed Time Observations for a total of 231.5 hours, split into 17 visits between 2022-11-13 and 2023-02-08 during which 3 transits of planet b, 9 transits of planet c and 8 transits of planet d were observed. An observation log of all available CHEOPS data is provided in Table 2. The undetrended CHEOPS light curves are visualised in Figure A.1.

We used the publicly available code chexoplanet[3] which jointly models both the TESS and CHEOPS photometry using the exoplanet library (Foreman-Mackey et al. 2021). For the TESS photometry, we used the PDCSAP photometry with two-minute cadence. Long-timescale trends, either systematic or from stellar rotation, were further removed using a cubic spline with breakpoints spacing of 0.9 days and in-transit data masked.

Since CHEOPS is in a nadir-locked orbit around the Earth, its field of view rotates around the target star once per 99-minute orbit. In combination with each background star having strongly asymmetric PSF (Benz et al. 2021), this can introduce flux modulation with roll angle. To reduce this modulation we used PIPE[4] (Brandeker et al. 2024) to extract PSF photometry (also see Morris et al. 2021; Szabó et al. 2021; Serrano et al. 2022, for more details on PIPE). To further take into account residual modulation, we used chexoplanet with two systematic removal steps. The first is to model linear and quadratic decorrelation of the flux with respect to various hyperparameters. In order to determine which decorrelation parameters are justified, chexoplanet first fits each individual CHEOPS light curve using all available hyper-parameter timeseries, which are normalised to have a mean $\mu = 0.0$ and a standard deviation $\sigma = 1.0$. This includes measured x and y centroid position, the first three aliases of the cos and sin of the roll-angle (for a detailed description of the roll-angle treatment see e.g. Lendl et al. 2020; Bonfanti et al. 2021), on board temperature $T$, background flux, major residuals of the PSF fit as found via PCA, and time itself (to account for flux trends in time, e.g. due to stellar activity). In the case of variables with noisy measurement which could add white noise to the flux such as the change in temperature $\Delta T$, their variation with time is fitted with cubic basis splines and both the high- and low-frequency variation are used as separate decorrelation parameters. A first step of Bayesian model comparison reveals which decorrelation parameters improve the model (we require a Bayes Factor >1), and a second step determines if these decorrelation parameters are similar across all observations (using leave-one-out comparison). The result is a series of linear and quadratic parameters which modify the CHEOPS flux according to the variation of a hyperparameter either for individual observations or globally. These are co-modelled with the transits.

Although both the PSF modelling and the detrending can remove the majority of the impact of systematics on the CHEOPS flux, the "spiky" PSF combined with the rapid field

---

[2] PAdova and TRieste Stellar Evolutionary Code: http://stev.oapd.inaf.it/cgi-bin/cmd

[3] https://github.com/hposborn/chexoplanet
[4] https://github.com/alphapsa/PIPE

**Table 2.** CHEOPS observation log for HIP 29442.

| ID | Start date (UTC) | Dur (hours) | File key | Av. eff. (%) | RMS (ppm) | Planets |
|----|------------------|-------------|----------|--------------|-----------|---------|
| 1 | 2022-11-13T09:51:58.566 | 13.23 | PR100031_TG054401_V0300 | 56 | 16.6 | c |
| 2 | 2022-11-16T15:20:12.607 | 22.07 | PR100031_TG054501_V0300 | 56 | 12.1 | c, d |
| 3 | 2022-11-22T01:33:34.389 | 18.18 | PR100031_TG054301_V0300 | 57 | 18.9 | b |
| 4 | 2022-11-27T14:08:14.891 | 10.13 | PR100031_TG054402_V0300 | 62 | 22.9 | c |
| 5 | 2022-11-29T09:56:19.658 | 13.76 | PR100031_TG054502_V0300 | 66 | 17.7 | d |
| 6 | 2022-12-05T15:56:56.577 | 18.64 | PR100031_TG054302_V0300 | 72 | 12.3 | b, d |
| 7 | 2022-12-22T06:24:00.725 | 11.45 | PR100031_TG054403_V0300 | 62 | 12.9 | c |
| 8 | 2022-12-25T04:12:40.557 | 14.84 | PR100031_TG054701_V0300 | 65 | 23.4 | d |
| 9 | 2022-12-25T19:17:41.222 | 10.79 | PR100031_TG054601_V0300 | 69 | 17.5 | c |
| 10 | 2022-12-29T08:57:59.537 | 10.88 | PR100031_TG054602_V0300 | 70 | 17.9 | c |
| 11 | 2022-12-31T13:33:58.633 | 14.24 | PR100031_TG054702_V0300 | 67 | 11.7 | d |
| 12 | 2023-01-02T00:54:58.150 | 11.98 | PR100031_TG054603_V0300 | 73 | 19.1 | b, c |
| 13 | 2023-01-06T23:41:52.550 | 12.97 | PR100031_TG054703_V0300 | 75 | 14.5 | d |
| 14 | 2023-01-12T11:51:42.819 | 10.55 | PR100031_TG054604_V0300 | 73 | 18.3 | c |
| 15 | 2023-01-19T22:52:03.617 | 14.95 | PR100031_TG054901_V0300 | 62 | 26.0 | d |
| 16 | 2023-02-06T06:16:57.508 | 10.49 | PR100031_TG054801_V0300 | 57 | 13.6 | c |
| 17 | 2023-02-08T04:11:27.804 | 12.37 | PR100031_TG054902_V0300 | 56 | 22.6 | d |

rotation often also results in sharp variations in flux as a function of roll-angle. However, such variation is typically extremely repeatable, and as hundreds of orbits of CHEOPS observations exist for HIP 29442, we can co-model these shorter-frequency variations with the transit model. To this end, `chexoplanet` uses a cubic spline with breakpoints spaced every 9 degrees (40 total splines for continuous data) common across all observations. The flux at each spline position therefore becomes an independent parameter to be co-modelled with the exoplanetary transits.

The transits were modelled using `exoplanet`, which samples the parameter space using the Hamiltonian Monte Carlo implementation, PyMC3 (Salvatier et al. 2016). The model used circular orbits, and limb-darkening parameters for TESS and CHEOPS were constrained to the expected theoretical values derived by Claret (2017, 2021) respectively. Planetary radius ratios were fitted using a broad log-Normal prior. Impact parameters were fitted using the prior of Espinoza (2018). To account for additional white noise, jitter terms were also included for each instrument (TESS and CHEOPS) with broad log-Normal priors. Initial fits to TESS and CHEOPS photometry revealed inconsistencies in the depth, duration and timing, especially for planet d. As a compromise between a full photodynamical TTV model (which struggles due to the low per-transit S/N of the planets) and a linear ephemeris model, we modelled periods split across the TESS and CHEOPS data for all three planets. The resulting photometric fits can be seen in Figure 1, while the derived planetary parameters are listed in Table 3.

### 3.2. Radius discrepancies with *Damasso et al. (2023)*

Damasso et al. (2023) used TESS photometry to reveal radii of $3.48 \pm 0.07$, $1.58 \pm 0.10$ and $1.37 \pm 0.11$ $R_\oplus$ for planets b, c, and d respectively. This suggested the inner-most planets c and d were significantly ($\sim 2\sigma$) different in radius, with the middle planet being the smallest. Our analysis based on a higher-quality dataset of TESS and CHEOPS photometry found radii of $3.410 \pm 0.046$, $1.551 \pm 0.045$ and $1.538 \pm 0.049$ $R_\oplus$. Hence, we found $<1\sigma$ agreement for planets b and c. For planet d, our value and error are $\sim 3.4\sigma$ larger than the median value of Damasso et al. (2023),

although only $\sim 1.5\sigma$ using their larger uncertainties. The resulting difference in mass and radius is also visualised in Figure 2. We note that Damasso et al. (2023) were aware of the limitations of their radius measurements given the low per-transit S/N in the TESS light curves, and adopted a $3\sigma$ confidence interval for example for their internal structure modelling. The 8 transits observed by CHEOPS more than double the number of transits of planet d observed by TESS, greatly boosting the S/N. We are also helped by observing these transits within a single observing season, while the TESS observations were separated by two years and therefore were more at risk of ephemeris drift due to transit timing variations. Although an analysis using each transit time as a free parameter did not reveal any significant TTVs with amplitudes above 1 h, our split period modelling between TESS and CHEOPS did reveal a $1.5\sigma$ drift in period between the two datasets. We also found such a split period model produced a better phase-folded transit fit to the TESS and CHEOPS datasets. We attempted to split the model into three parts - one for each of the TESS sectors plus CHEOPS but found that doing so resulted in no clear detection of a periodic transit signal at the expected ephemeris in the first TESS sector, due the lower S/N from only three transits. HIP 29442 d therefore shows that caution is required when determining the radii of small planets from multi-year TESS photometry when the per-transit S/N is low and there are significant gaps between observations.

### 3.3. Radial velocities

Damasso et al. (2023) analysed 83 spectra of HIP 29442 collected with ESPRESSO, reporting RV semi-amplitudes of $2.8 \pm 0.2$, $2.1 \pm 0.1$ and $1.9 \pm 0.1$ m s$^{-1}$ and masses of $9.6 \pm 0.8$, $4.5 \pm 0.3$ and $5.1 \pm 0.4$ $M_\oplus$ for HIP 29442 b, c, and d respectively. There are also 71 additional Keck-HIRES RVs presented by Akana Murphy et al. (2023), who report an RV semi-amplitude of $1.62 \pm 0.67$ m s$^{-1}$ and a mass of $5.8 \pm 2.4$ $M_\oplus$ for planet b. We re-ran the model from Damasso et al. (2023) using our updated ephemeris and including both the ESPRESSO and Keck-HIRES RVs. The best-fit RV model for all three planets is plotted in Figure 3 along with the RV Doppler signals from both datasets. The error bars are inflated, accounting for the uncorrelated jitter
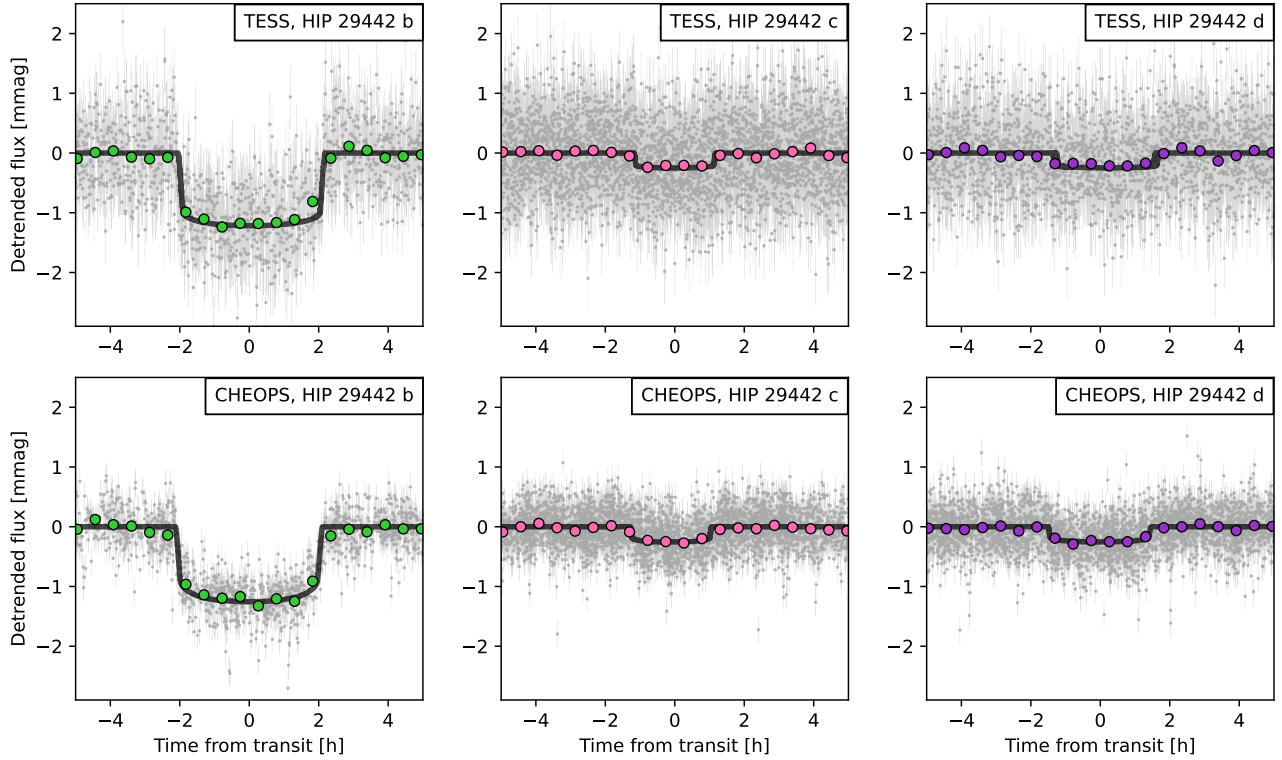
**Fig. 1.** Detrended TESS (top row) and CHEOPS (bottom row) light curves, phase-folded to the orbital periods of HIP 29442 b (left), c (middle), and d (right). The coloured points show the 30 min binned data; the solid black lines show the best-fit transit models.

**Table 3.** Posterior distributions of the planetary parameters for planets b, c, and d.

| Parameter | HIP 29442 b | HIP 29442 c | HIP 29442 d |
|---|---|---|---|
| Epoch, $t_0$ (BJD-2 457 000) | 2 458 474.56927 ± 0.00084 | 2 458 471.3600 ± 0.0033 | 2 458 472.9865 ± 0.0051 |
| Period, $P$ (d) | 13.6308205 ± 0.0000090 | 3.5379559 ± 0.0000082 | 6.429575 ± 0.000026 |
| Semi-major axis, $a$ (AU) | 0.1110 ± 0.0020 | 0.04518 ± 0.00082 | 0.0673 ± 0.0012 |
| Semi-major axis over stellar radius, $a/R_s$ | 23.88 ± 0.43 | 9.72 ± 0.18 | 14.5 ± 0.26 |
| Transit duration, $t_D$ (h) | 4.327 ± 0.022 | 2.429 ± 0.060 | 3.08 ± 0.12 |
| Radius ratio, $R_p/R_s$ | 0.03195 ± 0.00032 | 0.01453 ± 0.00040 | 0.01440 ± 0.00044 |
| Radius, $R_p$ ($R_\oplus$) | 3.410 ± 0.046 | 1.551 ± 0.045 | 1.538 ± 0.049 |
| Incident flux, $S_p$ (kW m$^{-2}$) | 74.7 ± 5.1 | 451 ± 31 | 203 ± 14 |
| Equilibrium temp., $T_{eq}$ (K) | 716 ± 12 | 1123 ± 19 | 920 ± 16 |
| Impact parameter, $b$ | 0.273 ± 0.072 | 0.514 ± 0.047 | 0.443 ± 0.090 |
| RV semi-amplitude $K$ (m s$^{-1}$) | $2.63^{+0.20}_{-0.19}$ | 2.04 ± 0.11 | 1.91 ± 0.12 |
| Mass $M_p$ ($M_\oplus$) | $9.10^{+0.82}_{-0.79}$ | 4.50 ± 0.32 | 5.14 ± 0.41 |

terms. The resulting RV semi-amplitudes and planetary masses are presented in Table 3. They are in good agreement with the values presented in Damasso et al. (2023).

### 3.4. The planets of the HIP 29442 system within the exoplanet population

Figure 4 shows the planets of the HIP 29442 system in the context of the population of small exoplanets, in terms of their planetary radii and orbital periods. This plot was generated using the updated version of the PlanetS catalogue of transiting exoplanets with reliable mass and radius values (initially introduced by Otegi et al. 2020a, available on DACE[5]). We can

see that HIP 29442 c and d lie below the radius valley (plotted using the fit from Ho & Van Eylen 2023, for the stellar mass of HIP 29442), while HIP 29442 b not only lies above the radius valley but actually beyond the radius cliff found at around 3 $R_\oplus$ in the *Kepler* data (Fulton & Petigura 2018). One of the most popular explanations for the radius cliff in the literature is the fugacity crisis hypothesis presented by Kite et al. (2019). They showed that starting from planetary radii of around 3 $R_\oplus$, the pressure at the base of a hydrogen-dominated atmosphere becomes high enough for the hydrogen to dissolve into the magma below, thus inhibiting further planet growth. Other works also suggested more weakly bound atmospheres at higher planetary masses (Owen & Wu 2017) and the timing of atmospheric accretion (Lee & Chiang 2016) as possible explanations. More
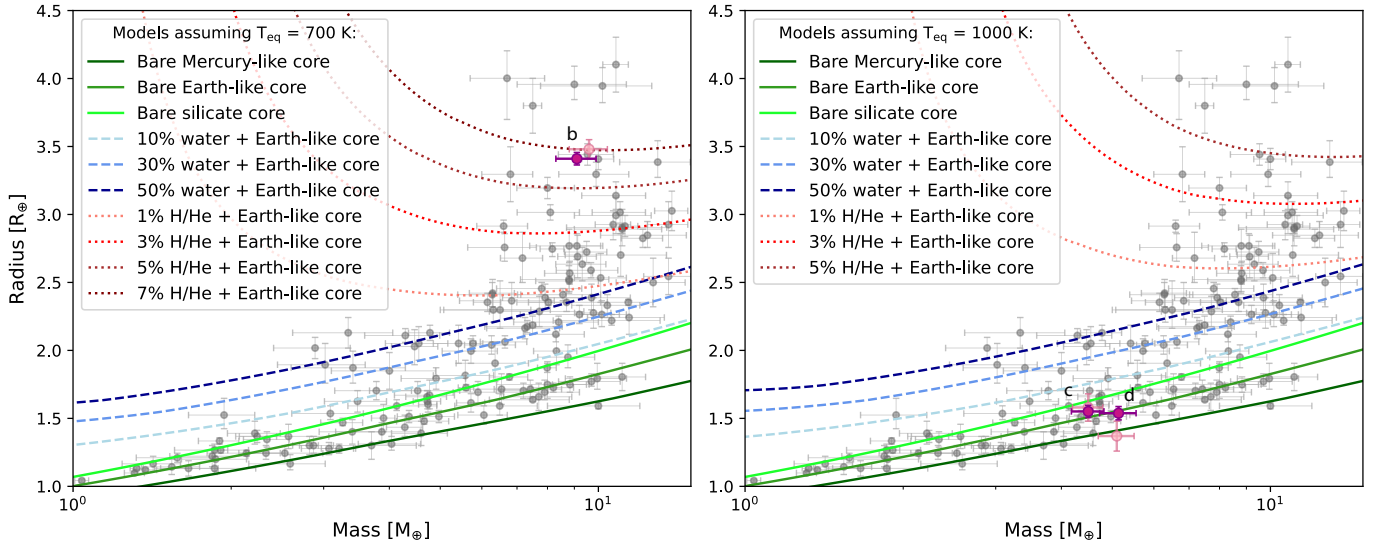
---

[5] https://dace.unige.ch/exoplanets

**Fig. 2.** Mass-radius diagrams showing the locations of HIP 29442 b (left panel) and HIP 29442 c and d (right panel) in relation to the known exoplanet population. The transparent pink points show the planetary parameters derived by Damasso et al. (2023). Mass-radius relations for fixed compositions and equilibrium temperatures were generated using BICEPS (Haldemann et al. 2024). Shown are three different compositions for bare cores (solid lines in different shades of green), Earth-like cores with different amounts of water (dashed lines in different shades of blue) and Earth-like cores with different amounts of H/He (dotted lines in different shades of red). The models in the left panel were calculated assuming an equilibrium temperature of 700 K (similar to HIP 29442 b), while the models in the right panel were calculated assuming an equilibrium temperature of 1000 K (similar to HIP 29442 c and d).

recently, Burn et al. (2024) also reproduced the radius cliff using a combined planet formation and evolution model for planets with fully mixed H/He and water envelopes.

## 4. Internal structure analysis

As a first step in analysing the interior composition of the planets in the HIP 29442 system, we look at their location in a mass-radius diagram as shown in Figure 2. We find that planets c and d lie close to the mass-radius relation for a bare Earth-like core (right panel). Meanwhile, planet b lies well above the 50% water line, generated assuming an Earth-like core and an equilibrium temperature similar to HIP 29442 b, and therefore seems to host an envelope with at least some H/He (left panel). All mass-radius relations were generated using the forward model of the BICEPS code (Haldemann et al. 2024). However, as determining the internal structure of an exoplanet from its radius and mass is a highly degenerate problem, we describe how we ran a full Bayesian inference model for all three planets in the following section. The high precision of the radii and masses we have derived in Section 3 provides us with ideal circumstances to do so.

### 4.1. Previous work

In past work (e.g. Leleu et al. 2021; Lacedelli et al. 2022; Wilson et al. 2022; Luque et al. 2023), we have used an inverse method based on the work of Dorn et al. (2015, 2017) to derive posterior distributions for the internal structure parameters of each planet, which was introduced and reviewed in detail in Leleu et al. (2021). As in Dorn et al. (2015, 2017), our framework is split into two main parts: a forward model that calculates the radius of a planetary structure with a given mass, composition and external conditions, and a Bayesian inference algorithm used to sample the parameter space of possible internal structure parameters. These sampled parameters are then passed to the forward model, which allows us to compare the calculated radii of

the sampled planetary structures to the observationally derived radius, or more precisely to the derived transit depth. This general approach is also used in other works, for example by Acuña et al. (2021) and Haldemann et al. (2024).

To make the use of such an inverse method feasible even with a quite computationally expensive forward model, these other works use Markov chain Monte Carlo (MCMC) or nested sampling as their Bayesian inference algorithms. What differentiates our internal structure modelling framework `plaNETic`[6] from them is the use of a deep neural network (DNN) that is trained on data generated with the chosen forward model, a method first introduced in this context by Alibert & Venturini (2019). This DNN is then used to replace the forward model in the Bayesian inference scheme, taking the same input parameters as the forward model and using them to calculate the radii of the sampled planetary structures, but speeding up the calculation by more than four orders of magnitude. This extensive decrease in computation time allows us to use a brute-force full grid sampling approach for the Bayesian inference scheme, while still speeding up the computation of the posterior distributions of the internal structure parameters for the individual planetary systems. Other works such as Baumeister et al. (2020) and Haldemann et al. (2023) also use neural networks to speed up the calculation of planetary internal structures. The difference to our model is that they replace the entire Bayesian framework with a neural network and not just the forward model. This means that their methods can compute posteriors for the internal structure of a planet faster than ours, but they also do not allow for changes in the used inference method, such as the used priors.

The new version of `plaNETic` introduced in this work is publicly available and can be adapted for any choice of forward model, all that is necessary is training a DNN on the desired model. By default, `plaNETic` uses DNNs trained on the planetary structure model of BICEPS (Haldemann et al. 2024), as
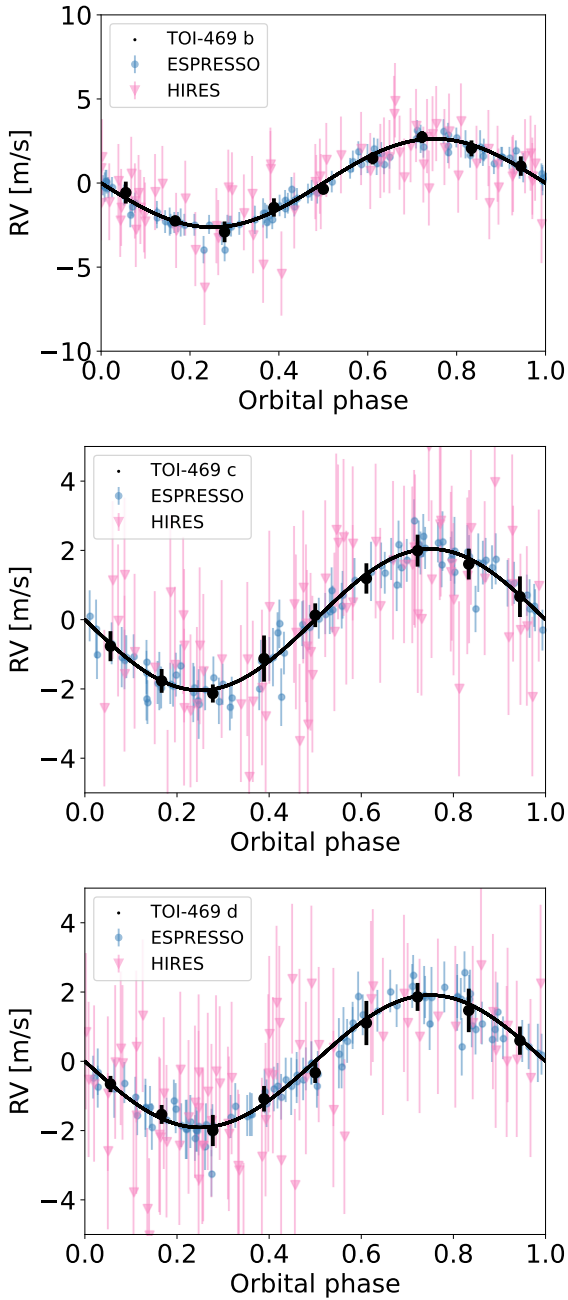
---

[6] https://github.com/joannegger/plaNETic

**Fig. 3.** Radial velocities vs orbital phase for HIP 29442 b (top), c (middle), and d (bottom), including the datasets from ESPRESSO (Damasso et al. 2023, round markers in blue) and HIRES (Akana Murphy et al. 2023, triangle markers in pink). The best-fit model is shown in black.
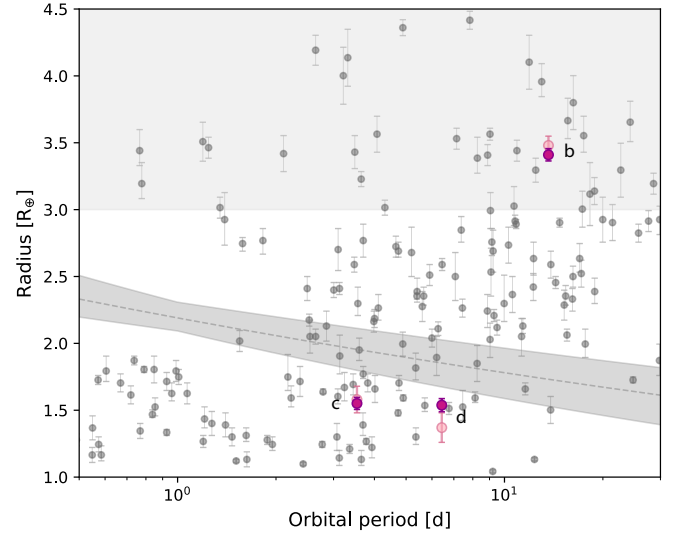


**Fig. 4.** Location of the HIP 29442 planets (purple markers) in the orbital period-radius diagram in relation to the known exoplanet population, plotted using the PlanetS exoplanet catalogue. The transparent pink points show the planetary parameters derived by Damasso et al. (2023). The location of the radius valley is indicated in dark grey using the fit from Ho & Van Eylen (2023). The area shaded in light grey is the radius cliff beyond 3 $R_\oplus$.

described in detail in Section 4.2. In the following, we first briefly summarise the specifics of the model used in past work.

In the preliminary version of `plaNETic` introduced in Leleu et al. (2021), a simple structure model is used as the forward model. Each planet is assumed to be built up of four distinct layers. The innermost layer consists of an inner iron core with a molar fraction of up to 19% of sulphur, used as a placeholder for any lighter elements in the core (modelled using the equations of state (EoS) from Hakim et al. 2018). On top of this core, a silicate mantle made up of oxidised silicon, magnesium and iron (EoS from Sotin et al. 2007) is added. Next, we add a condensed water layer (EoS from Haldemann et al. 2020) with fixed outer boundary conditions of $P = 1$ bar and $T = 300$ K. On top of this

structure, a pure H/He envelope is modelled separately according to the fit from Lopez & Fortney (2014). A DNN with 6 hidden layers of 2048 units each was then trained on a large database with 5 million points generated with this forward model. The accuracy of this DNN was investigated in detail in Leleu et al. (2021), with the study showing an error on the predicted radius that is lower than 0.4% in 99.9% of the cases.

For each planet in the system, 100 million different combinations of internal structure parameters are sampled, with a uniform prior for the mass fractions of the inner iron core, silicate mantle and water layer (on the simplex on which they add up to unity) and a log-uniform prior for the mass of H/He added on top. Additionally, we introduced an upper limit of 0.5 for the water mass fraction in accordance with Thiabaud et al. (2014) and Marboeuf et al. (2014). All planets in the system are then modelled simultaneously in order to leverage the correlation between the observed properties of the different planets in the system, which stems from the fact that both the planetary mass and radius are measured in relation to the host star. This interdependency of the mass and radius values of planets in the same system is also considered by Dorn et al. (2018), who run a resampling scheme after inferring the structure of the individual planets as opposed to modelling all planets simultaneously. Furthermore, we followed Thiabaud et al. (2015) and assumed that the Si/Mg/Fe ratios of all planets in the system are identical and match the ones calculated from the stellar abundances exactly for this previous version of the model.

### 4.2. Internal structure modelling framework

#### 4.2.1. Forward model

In this work, we now introduce a new and improved version of `plaNETic`. As a first change compared to the previous version, we use the planetary structure model of BICEPS (Haldemann et al. 2024) as our forward model, which allows for a significant increase in physical accuracy compared to the previously used

structure model. BICEPS does include not only this planetary structure model but also an MCMC-based Bayesian inference code. However, this part of the code is not used here.

As before, each planetary structure is built up of an inner core, mantle and volatile layer. For the core and mantle layers, the structure model of BICEPS uses an expansive collection of EoS that allows for both solid and molten phases. In principle, BICEPS allows for any combination of a pure water layer with a possibly water-enriched H/He envelope. For this work, we use a model setup where the volatile layer is a uniformly mixed envelope of water and H/He with no pure water layer present. This volatile layer is modelled self-consistently with the rest of the planet and is split into two distinct sub-layers, an irradiated outer atmosphere and an envelope with almost all stellar flux already absorbed in the layer above. The irradiated atmosphere is modelled using the non-grey analytical atmosphere model of Parmentier & Guillot (2014) and Parmentier et al. (2015) together with the opacity grid of Freedman et al. (2014). As the used atmosphere model depends on the intrinsic luminosity of the modelled planet, a quantity that especially for small planets usually cannot be measured directly, we use the age-luminosity relation from Mordasini (2020). This relation is a fit of coupled formation and evolution calculations as presented in Mordasini et al. (2012), but also includes the cooling model of the solid core from Linder et al. (2019). Whether the envelope follows a convective or radiative profile is determined self-consistently using the Schwarzschild criterion. Condensation is not taken into account, since the planets of the HIP 29442 system are on close-in orbits and therefore have high equilibrium temperatures. Finally, the transit radius is defined as the radius where the chord optical depth is $\tau_{ch}$ = 2/3 (Guillot 2010). For a more detailed description of the planetary structure model of BICEPS including the full list of used EoS, we refer to Haldemann et al. (2024).

In the subsequent sections, we use the following notation to refer to the internal structure parameters introduced above: $w_{layer}$ denotes the mass fraction of a given layer with respect to the entire planet, while $Z_{envelope}$ is defined as the mass fraction of water in the volatile layer. Finally, $x_{element,layer}$ denotes the molar fraction of a given element in the specified layer.

## 4.2.2. Inference algorithm and priors

The inference method implemented in `plaNETic` is a full-grid acceptance-rejection sampling algorithm. As a first step, 10 000 synthetic stars are sampled from the previously observationally derived distributions of the relevant stellar properties ($R_\star$, $M_\star$, $t_\star$, $T_{eff}$, [Si/H], [Mg/H] and [Fe/H]), listed in Table 1 for HIP 29442. For each of these synthetic stars, 10 000 synthetic planetary systems are then sampled. This is done by sampling RV semi-amplitudes and orbital periods from the observationally derived distributions, as summarised in Table 3 for the HIP 29442 planets. We also simultaneously sample all relevant internal structure parameters from the chosen priors for each planet in the system. Based on these sampled parameters for both the star and the planets in the system, the neural network trained on the forward model is then used to calculate the transit depths that these synthetic planets would have. Each synthetic planet is then compared to the derived distribution of the transit depth for the observed equivalent planet and either accepted or rejected based on the calculated likelihood of the two agreeing. By modelling all planets in the system simultaneously and using transit depths and RV semi-amplitudes instead of radii and masses directly, we ensure that all synthetic planets orbit exactly

the same star (not just within the error intervals) and include the correlation of the planetary radii and masses of planets in the same system.

For the priors of the mass fractions of the different layers (inner core, mantle and envelope) and the composition of these layers (molar fractions of Fe and S for the inner core; oxidised Si, Mg and Fe for the mantle; water and H/He for the envelope), we consider different scenarios. In the first case (hereafter case A), we use a prior for the mass fractions of the inner core layer, mantle layer and the total water mass fraction in the planet that is uniform on a simplex on which they add up to 1, while still assuming an upper limit of 0.5 for the accreted water (Thiabaud et al. 2014; Marboeuf et al. 2014). Additionally, we then use a log-uniform prior for the accreted H/He. After sampling the mass fraction of accreted H/He, the mass fractions of the inner core, mantle and water are then rescaled so that the sum of these four mass fractions equals unity. These priors are motivated by the assumption that the planet has formed outside the iceline, which means that it has accreted water not only through the accreted gas but has also accreted icy planetesimals. Even though this scenario assumes that water is accreted in the form of ice, it is assumed that the total amount of water sampled is located in the envelope and uniformly mixed with the sampled amount of H/He for the calculation of the internal structure of the planet.

Conversely, for the second case (case B), we assume that the planet formed inside the iceline. This means that any water present comes from the gas the planet has accreted. In this case, we use a uniform prior to sample the mass fraction of the inner core and calculate the corresponding mass fraction of the mantle layer as 1 minus the core mass fraction (both with respect to the total mass of refractories in the planet). We also apply a log-uniform prior for the mass fraction of the accreted gas envelope. Finally, we sample the mass fraction of water with respect to the total mass of the gaseous envelope using a Gaussian prior with a mean of 0.5% and a standard deviation of 0.25%, in accordance with the molecular abundance of water in the solar nebula (Mousis et al. 2009; Lodders 2003). This means that an envelope composition of 1× solar (Fortney et al. 2013) is enclosed within the 3 sigma interval. We then again re-scale the mass fraction of the inner core and mantle layers so the sum of all three layers add up to unity.

In a second step, we also consider different options for sampling the planetary Si/Mg/Fe ratios (for both case A and case B described above). On the one hand, Thiabaud et al. (2015) used a combined chemical and planet formation model and found that the elemental Si/Mg/Fe ratios in planets are essentially identical to the ones of their host star. Similarly, Pelletier et al. (2023) measure abundances of refractory elements in the giant planet WASP-76 b and find them mostly stellar-like. This assumption is also frequently used in other internal structure modelling frameworks, such as Dorn et al. (2017), Acuña et al. (2021) and our own past work (e.g. Leleu et al. 2021; Lacedelli et al. 2022; Wilson et al. 2022; Luque et al. 2023). On the other hand, Adibekyan et al. (2021) also find a correlation between the composition of rocky exoplanets and their host stars. However, according to their study planets seem to be enriched in iron compared to their host stars. Other studies indicate similar findings (e.g. Liu & Ni 2023). Guimond et al. (2024) also provide a thorough review on the processes through which stellar and planetary compositions are related. In the following, we use three different options for our compositional priors: (1) assuming the planetary Si/Mg/Fe ratios to match the stellar ones exactly, (2) implementing the iron-enriched planetary Si/Fe and Mg/Fe ratios using the relation by Adibekyan et al. (2021) while keeping the

stellar Si/Mg ratio, and (3) sampling the elemental abundances of Si, Mg and Fe in the planet uniformly from a simplex, without taking into account stellar abundances. For the last option, we add an upper limit of 0.75 for the amount of Fe compared to Si and Mg in the planet, similar to Acuña et al. (2021). The reasoning behind this is that a planet made up of pure iron with a volatile layer on top is not physical from a planet formation perspective. We do note, however, that this would not apply if one were to model a super-Mercury like planet (such as GJ 367 b, Goffo et al. 2023).

### 4.2.3. Training DNNs to replace the forward model

As for the previously used model version, we trained DNNs for this improved forward model to reduce the necessary computation time. As in the previous version of `plaNETic`, the DNNs used here are conventional feed-forward neural networks with a layer of input neurons, multiple hidden layers and one output neuron. The output of such a neural network is calculated layer by layer, starting with the input layer which receives a set of physical values as input. The value of each neuron in the next layer is then determined as a linear combination of the values and weights of the neurons in the previous layer. To also allow for non-linearity, an activation function is then used to calculate the neuron's value. Training a neural network means the process of iteratively improving the weights of all neurons based on a set of training data, so that the value of the output neuron approaches the expected value for each set of input parameters. The discrepancy between the values that the output neuron gives and the target values is measured with the so-called loss function, which is minimised during training (Bishop 2006; Goodfellow et al. 2016).

In contrast to this, Baumeister et al. (2020) and Haldemann et al. (2023) use more complex forms of neural networks (more specifically mixture density networks and conditional invertible neural networks). This is necessary because they solve the inverse problem directly using their neural networks, while we only replace our forward model.

To account for the increased complexity of the structure model with this new version of `plaNETic` and still reach a similar accuracy as before, we now trained separate DNNs for different mass regimes: (M1) 0.5–6 $M_\oplus$ and (M2) 6–15 $M_\oplus$. We also trained DNNs for a third mass regime (M3) that will be used in future work for planets with masses between 15 and 30 $M_\oplus$. For each mass regime, we generated two different large databases of 15 million internal structure models, one corresponding to an envelope with high water-enrichment (consistent with case A above) and one corresponding to a H/He envelope enriched with 0-1% of water in mass (consistent with case B above). To create the databases, the internal structure parameters and boundary conditions were randomly sampled using the same set of priors as will be used when later inferring the internal structure of a planet. The transit radii of the sampled structures are then calculated using the planetary structure model of BICEPS (Haldemann et al. 2024).

Each database was then split randomly into 80% training data, 10% validation data and 10% test data. Using the Python library `tensorflow` (Abadi et al. 2015), we then used each database to train a DNN. To this end, the input parameters of the training dataset were first normalised feature-wise (i.e. each input parameter was scaled by dividing by the mean and subtracting the standard deviation of the distribution of the parameter in question). The individual layer mass fractions and molar fractions describing the composition of the core and mantle layers

respectively are not independent of each other but always need to add up to 1. For this reason, only the layer mass fractions of the inner core, water and H/He are used for training the neural networks, as well as the molar fractions of sulphur in the core and silicon and magnesium in the mantle (but not the mantle mass fraction and the molar fractions of iron in the core and in the mantle). Overall, the neural network therefore has nine input neurons, corresponding to the equilibrium temperature of the planet, the atmospheric water mass fraction, the intrinsic luminosity of the planet (derived from the stellar age), the mass of the planet, the mass fractions of the inner core and the envelope with respect to the total planet mass, the molar fraction of sulphur in the inner core and the molar fractions of silicon and magnesium in the mantle. For both the envelope mass fraction and the intrinsic luminosity, we look at the quantities in log-space. Conversely, each DNN has a single output neuron with a linear output activation function that estimates the transit radius of the sampled structure.

For each database, we tried a range of different network architectures, which we then compared using the validation data. We chose the best DNN based on the number of data points in the validation data with a prediction error, defined as $\frac{R_{DNN} - R_{BICEPS}}{R_{BICEPS}}$, of more than 3% (the radius precision usually reached when characterising a planet with CHEOPS). The final network architectures for each mass regime and water accretion option are summarised in Table B.1. To allow for non-linearity, the standard ReLU function (given by $\text{ReLU}(x) = \max(x, 0)$; Nair & Hinton 2010) was used as an activation function for each unit. Each DNN was trained for a maximum of 10 000 training epochs with early stopping activated if no improvement was seen for 100 epochs to avoid overfitting. For all DNNs, this happened after training for between 400 and 1100 epochs. We used the mean square error of the transit radius as our loss function and fit the DNNs using the ADAM optimiser (Kingma & Ba 2015) with a learning rate starting at 0.001 that is reduced by a factor 2 each time the validation loss reaches a plateau for 30 training epochs. Since our databases are too large to fit into memory at once, we used a data generator for both the training and validation data that randomly selects batches of 1024 data points that are then used for training and validation.

### 4.2.4. DNN performance

We now used this new version of `plaNETic` to calculate posterior distributions of the internal structure parameters for HIP 29442 b, c, and d, using both water priors (cases A and B) and all three compositional priors for the elemental Si/Mg/Fe ratios (options 1, 2 and 3) discussed above. However, before discussing the results of these models, we test the performance of our DNNs by randomly choosing 100 structures from each posterior of each planet and running the full forward model of BICEPS for them. The resulting distribution of the prediction error of the DNNs on the transit radius of each structure is shown in Figure 5, for each planet and water prior separately, but combined for the three Si/Mg/Fe prior choices. In all cases, the median values of the distributions lie between −0.13 and 0.11% with the 16th percentiles above −0.40% and the 84th percentiles below 0.60%. These prediction errors are well below the observational errors on the radii.

We also tested how much the use of DNNs speeds up the calculation of the transit radii of the same randomly sampled structures as compared to the full forward model. The full results of this test can be found in Table B.2. To briefly summarise our

**Table 4.** Overview of the different versions of `plaNETic` used to model the internal structure of HIP 29442 b, c, and d.

| Model | EoS | Volatile layer | Water prior | Si/Mg/Fe prior |
|---|---|---|---|---|
| A1 A2 A3 | Full set of EoS from BICEPS | Uniformly mixed H/He and water envelope | Accreted as solids | stellar iron-enriched free |
| B1 B2 B3 | Full set of EoS from BICEPS | Uniformly mixed H/He and water envelope | Accreted as gas only | stellar iron-enriched free |
| PREV | Limited set of EoS [1], [2], [3] | Condensed water layer, separately modelled H/He envelope [4] | Accreted as solids | stellar |

**References.** [1] Hakim et al. (2018); [2] Sotin et al. (2007); [3] Haldemann et al. (2020); [4] Lopez & Fortney (2014).
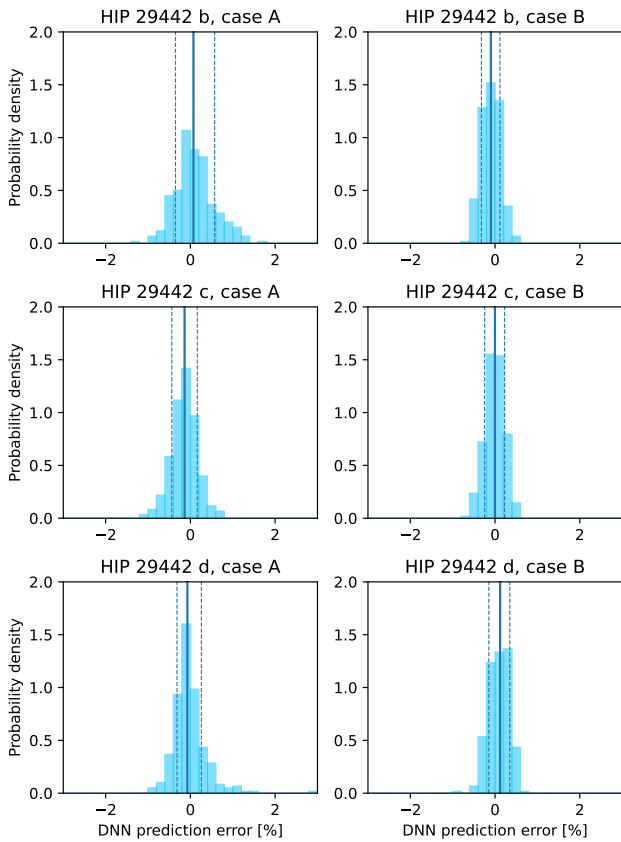


**Fig. 5.** Histograms of the DNN prediction error of the transit radius for 300 randomly sampled points in the posteriors, for each planet (rows) and both of the water prior options (columns). The vertical lines show the median and the 16th and 84th percentiles of each distribution.

findings, we can say that with the DNN, calculating the radii of 100 sampled structures takes around 0.035 seconds[7], while with BICEPS, calculating the same radii takes on average about 23 minutes for model A and 38 minutes for model B[8]. This is a speed-up of around a factor 40 000 for model A and a factor 63 000 for model B. What needs to be taken into account with this calculation, however, is of course also the computation time needed to generate the database necessary for training each DNN, which is around 5 days on 280 CPUs.

### 4.3. Results for HIP 29442 b, c, and d

For each planet, we ran a total of seven different interior models, six using the new version of `plaNETic` with the different priors for the water content and elemental Si/Mg/Fe ratios described in Section 4.2 and one using the old version of the code, which assumes a condensed water layer. Table 4 gives an overview of the different model versions used. The posterior distributions of the most important internal structure parameters for HIP 29442 b, c, and d are visualised in Figures 6, 7 and 8 respectively. The median values and one sigma errors of the posteriors of a wider range of parameters calculated for both the new and the old version of `plaNETic` are also listed in Tables B.3–B.6.

For HIP 29442 b, the results of the internal structure modelling depend significantly on whether we assume that the planet formed inside or outside the iceline. However, for one given water prior, the posteriors have similar median values for all three compositional priors for the planetary Si/Mg/Fe ratios. This is in agreement with the findings of Otegi et al. (2020b), who show that using stellar Si/Mg/Fe ratios as a proxy for the planetary composition does not always help to better constrain the internal layer mass fractions, especially for sub-Neptunes. Meanwhile, the spread of the distributions differs for the core and mantle mass fractions and, in the case of water prior B, to some extent also for the envelope mass fraction. However, for the core and mantle mass fractions, the posterior distributions are very close to the respective chosen priors (dotted lines). If we assume that HIP 29442 b was formed outside the iceline (case A), we find a broad posterior distribution for the planet's envelope mass fraction spanning almost the full range from 0 to 60%. The distribution of the envelope water mass fraction is a skewed Gaussian distribution that ranges from 0 up to almost 90%, with a mode of around 75%. If we assume that HIP 29442 b formed inside the iceline (case B), the posterior for the envelope mass fraction is much more tightly constrained with a peak at around 6%, which was to be expected as we significantly reduce the allowed compositional degeneracy in the envelope.

We can now compare this to the results from the previous version of our internal structure model, which assumes the planet to have a condensed water layer and models a pure H/He envelope independently of the rest of the planet. We limit this comparison to model A1 to ensure that both models use the same priors, both in terms of water content and Si/Mg/Fe ratios. We also use water
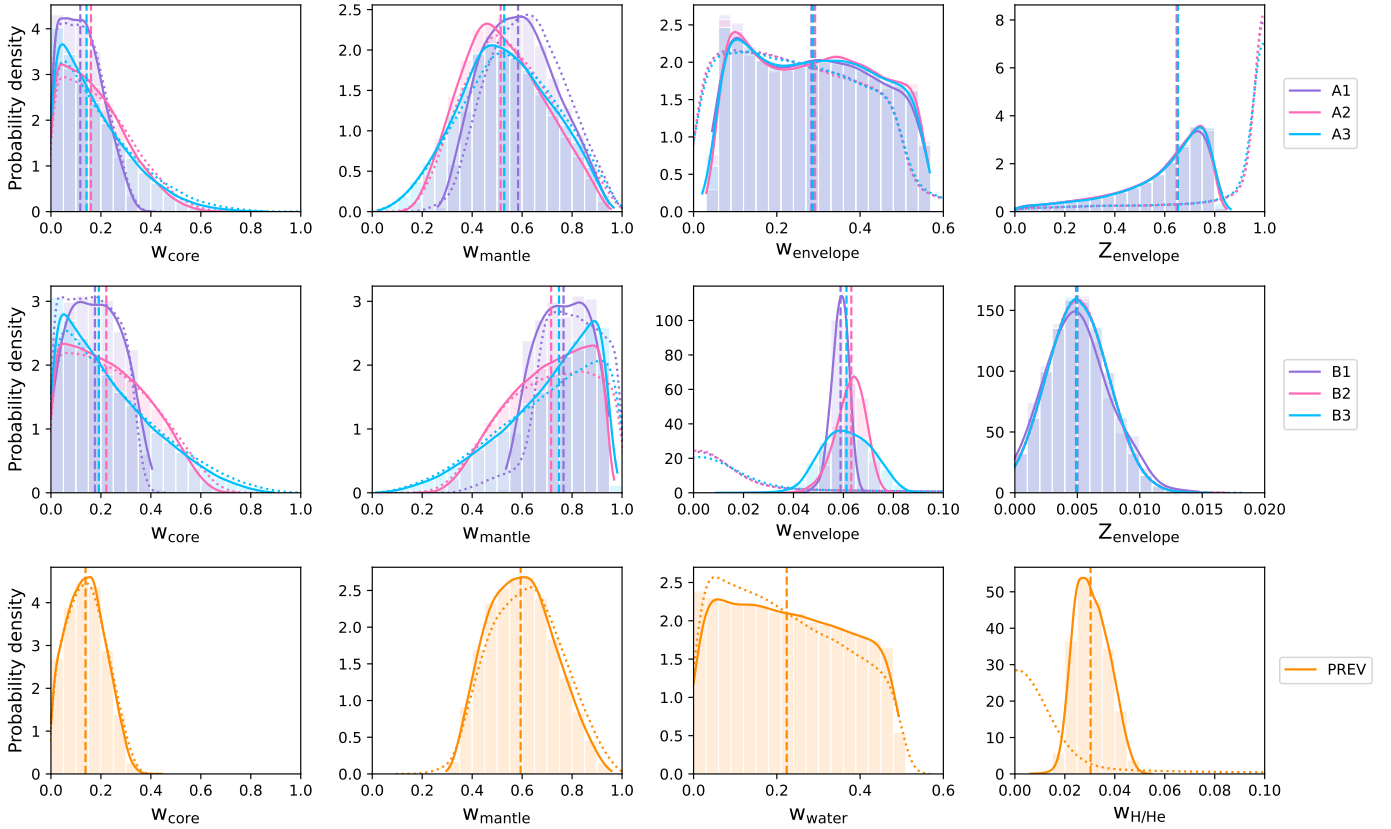
---

[7] Run on a 2021 MacBook Pro with an Apple M1 Pro chip.
[8] Run on a node of the HORUS cluster of the Theoretical Astrophysics and Planetary Science group at the University of Bern using $2 \times 14$-Core Intel Xeon Gold 6132 @ 2.6 GHz.

**Fig. 6.** Posterior distributions of the most important internal structure parameters for HIP 29442 b, namely the mass fractions of an inner core, mantle and envelope in the planet as well as the mass fraction of water in the envelope. The top row shows the posteriors assuming a prior consistent with the planet forming outside the iceline (case A), while the middle row uses a prior that is consistent with the planet forming inside the iceline (case B). For both water priors, we show the posteriors for three different compositional priors: first assuming that the planet has stellar Si/Mg/Fe ratios (purple), second assuming that the planetary bulk Si/Mg/Fe ratios are iron-enriched compared to the host star (pink) and third sampling the planetary bulk Si/Mg/Fe uniformly from the simplex on which the molar fractions add up to 1 (blue). The bottom row shows the posterior distributions of the mass fractions of an inner core, mantle, condensed water layer and separately modelled H/He envelope with respect to the total planet mass when applying the previously used version of the model assuming stellar Si/Mg/Fe ratios. The dashed vertical lines show the median value of each distribution. The dotted lines show the priors.

and H/He mass fractions with respect to the total planetary mass for both models, instead of using the total envelope mass fraction and envelope metallicity as shown in Figure 6 for models A1. For model A1, the water mass fraction for planet b is $18.4^{+16.1}_{-14.0}\%$, while the H/He mass fraction is $9.8^{+1.4}_{-3.0}\%$. For the previous model version, these values are $22.4^{+17.3}_{-15.6}\%$ for the water mass fraction and $3.0^{+0.8}_{-0.6}\%$ for the H/He mass fraction. The resulting water mass fractions for HIP 29442 b are therefore similar but slightly lower with the new and more physically robust model. Both distributions allow for a broad range of values. At the same time, we infer higher H/He mass fractions with the new model. The inferred core and mantle mass fractions are very similar for both model versions.

The resulting posterior distributions for the interiors of HIP 29442 c and d are very similar. Here, the posteriors of the core mass fractions are showing a trend of leaning towards the higher values covered by the priors for all three Si/Mg/Fe ratio options. For the mantle mass fractions, the same is true in the case of water prior A, while for water prior B, we observe the opposite effect for the iron-enriched and free Si/Mg/Fe priors. For both planets, we find that if they formed outside the iceline (case A), then their envelopes will mostly consist of water, with median values as high as 99.9% for the water mass fraction in the envelope and total envelope mass fractions between 0 and

20% depending on the chosen Si/Mg/Fe prior. In the formation scenario inside the iceline (case B), we find very small envelope mass fractions with median values between $10^{-6}$ and $10^{-5}$. If we again compare with the results from the previous model version, we can see that for both planet c and d, we also get H/He mass fractions that are negligibly small, while the water mass fraction is considerably larger than for case A1, which also uses a stellar Si/Mg/Fe prior and assumes that the planet accreted icy planetesimals outside the iceline. This result is expected, as we assume the water to be condensed and fix the temperature to 300 K at the water to H/He boundary in the previous model version. In conclusion, we find that planets c and d cannot have a H/He dominated envelope, as mass fractions as small as the ones our posteriors showcase would have quickly been lost through evaporation. If the planets do have an envelope, it needs to be of higher metallicity.

# 5. Hydrodynamic modelling

## 5.1. Model setup

To analyse what impact the different atmospheric compositions considered in Section 4 would have on the upper atmosphere's parameters and atmospheric mass loss, and hence also on the
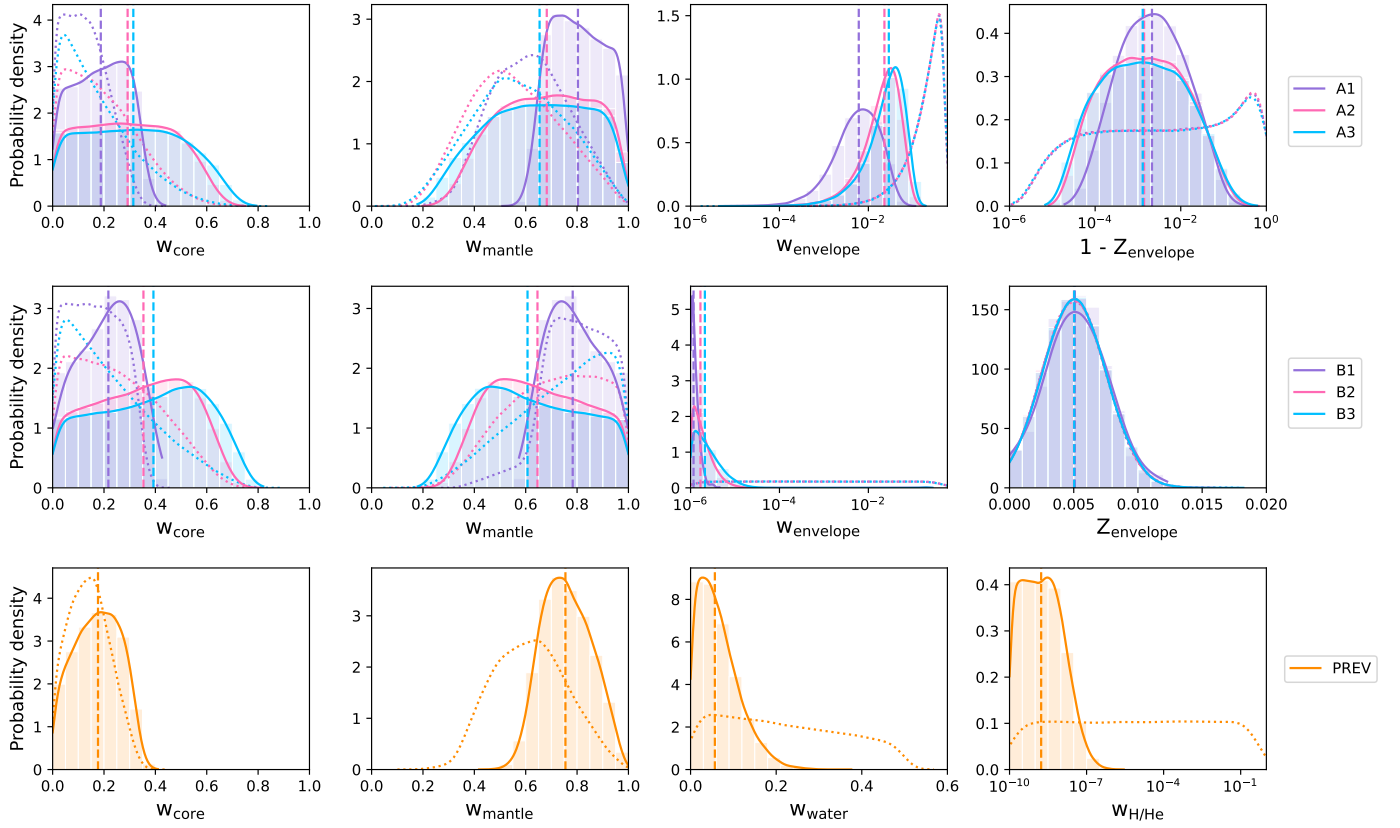
**Fig. 7.** Same as Figure 6 but for HIP 29442 c. The rightmost panel in the top row shows the H/He mass fraction instead of the water mass fraction in the envelope.
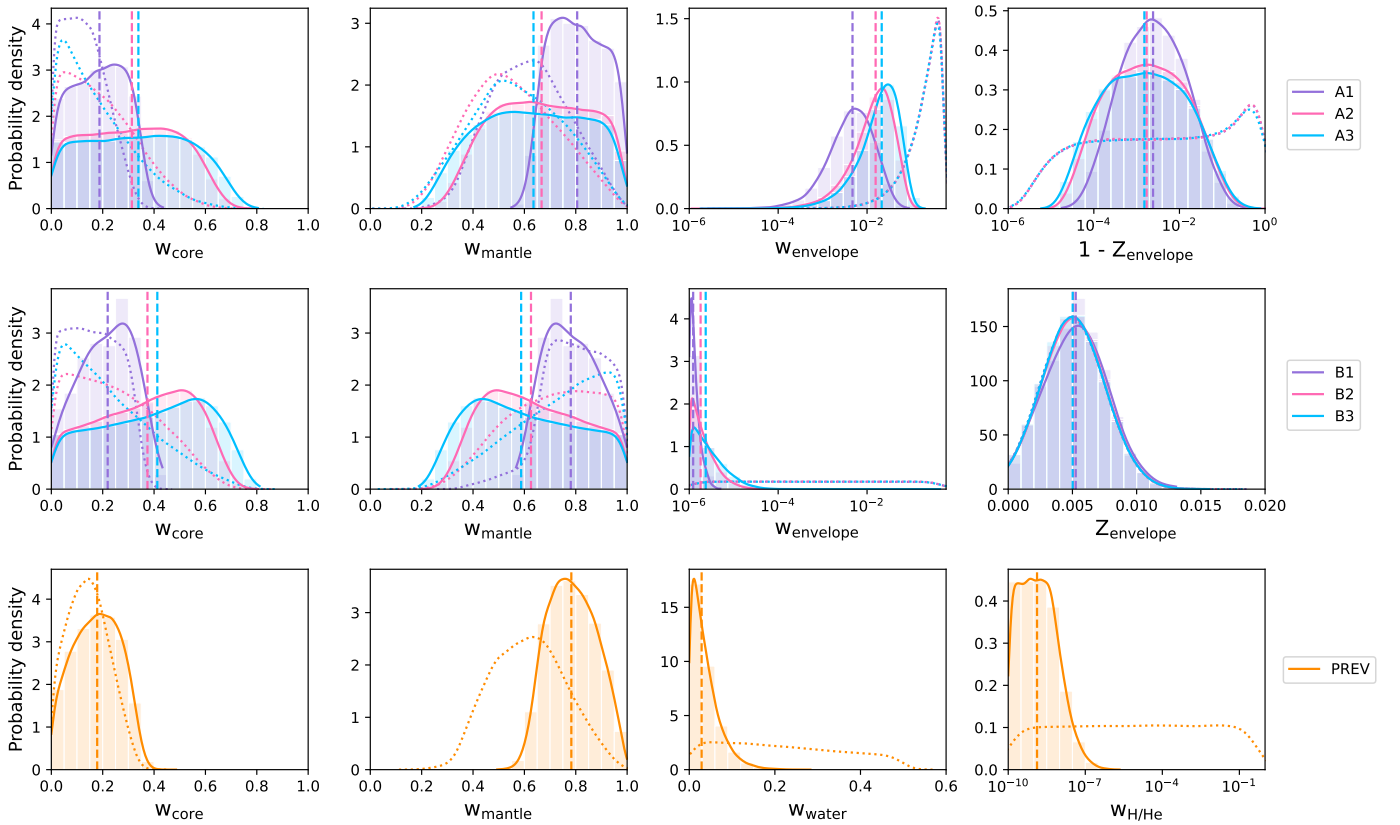


**Fig. 8.** Same as Figure 6 but for HIP 29442 d. The rightmost panel in the top row shows the H/He mass fraction instead of the water mass fraction in the envelope.

atmospheric evolution, we employ the 1D hydrodynamic model by Kubyshkina et al. (2024, Cloudy e Hydro Ancora INsieme; CHAIN). This code combines a 1D hydrodynamic upper atmosphere model based on that of Kubyshkina et al. (2018) with the non-local thermodynamical equilibrium (NLTE) photoionisation and radiative transfer code Cloudy (Ferland et al. 2017). The former is responsible for modelling the hydrodynamic outflow, while the latter solves the detailed (photo)chemistry and level populations for elements up to zinc, providing realistic heating and cooling functions. Given the flexibility of Cloudy in terms of gas compositions (the code supports switching on and off any element except for hydrogen and adjusting their abundances, allowing or prohibiting the formation of non-homogeneous molecules, and including dust), the CHAIN code allows modelling of a wide range of hydrodynamically escaping atmospheres. The hydrodynamic part assumes the atmosphere to be well-mixed within the simulation domain. This is an adequate assumption while the exobase level lies above the sonic point and is likely met by the majority of close-in exoplanets. We verify this during the simulation. Further, the atmosphere is treated as a uniform outflow with the mean molecular weight set by the employed composition.

The code accounts for the detailed spectral energy distribution (SED) of the host star and treats X-ray, extreme ultraviolet (EUV), and visible plus infrared (VIS+IR) parts of the spectra as separate sources set by their flux-wavelength dependence and the total flux within the given wavelength interval. To the best of our knowledge, no X-ray/EUV data is available for HIP 29442. Therefore, for our simulations, we employ the X-ray and EUV values predicted by the stellar evolution code Mors (Johnstone et al. 2021; Spada et al. 2013) for the age and mass of the star given in Table 1; we further scale the VIS-IR flux to the $L_{\text{bol}}$ of HIP 29442. For the shape of the spectrum, we employ that of a star of similar spectral type (i.e. HD 97658) provided by the Measurements of the Ultraviolet Spectral Characteristics of Low-mass Exoplanetary Systems survey (MUSCLES; France et al. 2016; Youngblood et al. 2016, 2017; Loyd et al. 2016, 2018). We briefly discuss the implications of choosing this specific spectrum at the end of the section.

Details concerning the code implementation and testing for hydrogen-helium atmospheres (with and without heavier elements in atomic form) can be found in Kubyshkina et al. (2024). In this study, we focus on comparing atmospheres with hydrogen-helium and water-rich compositions. As the simulations with CHAIN (particularly for water-rich atmospheres) are computationally expensive, we cannot perform them for the whole range of parameters predicted in Sections 3 and 4. Therefore, we employ the mean values from Table 3 for the radii, masses, orbital separations, and equilibrium temperatures of the planets in the HIP 29442 system. We note that these parameters were constrained well in the present study, and the variations within $1\sigma$ for planetary radius and orbital parameters are not expected to have any considerable effect on the predictions of CHAIN; the variations in mass can lead to changes in the predicted atmospheric mass loss rates of about ~10%. For each of the planets, we further consider two limiting cases: pure hydrogen-helium atmospheres with stellar metallicities (further referred to as H/He atmospheres) and the posteriors of model A1 (water accreted in the form of ice and stellar Si/Mg/Fe ratios; further referred to as $H_2O$ atmospheres). More specifically, the latter denotes atmospheric water mass fractions of ~65% for the outermost planet b and of ~99% for the inner planets c and d. We tested our models for different metallicities and found that for all the planets in the HIP 29442 system, the variations in Si/Mg/Fe

**Table 5.** Atmospheric loss rates predicted for planets HIP 29442 b, HIP 29442 c and HIP 29442 d by CHAIN.

| Planet | Model* | X-ray+EUV (erg/s/cm$^2$) | escape rate ($10^{33}$/s) | mass loss rate ($10^9$ g/s) |
|--------|--------|--------------------------|---------------------------|------------------------------|
| b | H/He | 703.6 | 2.21 | 4.80 |
| b | $H_2O$ | 703.6 | 0.43 | 2.01 |
| c | H/He | 4250 | 13.95 | 30.27 |
| c | $H_2O$ | 4250 | 0.40 | 4.66 |
| d | H/He | 1917 | 0.66 | 1.43 |
| d | $H_2O$ | 1917 | 0.023 | 0.27 |

**Notes.** *H/He – hydrogen-helium atmospheres; $H_2O$ – atmospheres with large water fraction (model A1). The Si/Mg/Fe ratio is set to stellar values in both cases.

ratios considered in Section 4 have a minor effect on the results; therefore, we only consider here the case of atmospheres with stellar metallicity.

### 5.2. Atmospheric mass loss rates

From the hydrodynamic simulations, we found that in the case of H/He atmospheres, the general picture of the atmospheric outflow is rather similar for the two outer planets b and d: despite the density of planet b being ~4.25 times lower than that of planet d, in terms of the atmospheric escape, this is compensated by the planet's lower temperature and lesser X-ray/EUV fluxes at its orbit. Planet c, due to its shorter orbit, experiences stronger XUV heating and more intense outflow. We summarise the information about atmospheric escape from the planets in the HIP 29442 system in Table 5 and show the height profiles of their atmospheric temperatures and bulk outflow velocities in Figure 9, for both H/He and $H_2O$ atmospheric compositions. One can notice that the inclusion of large water fractions into the atmosphere does not have the same effect for different planets, and the effect does not solely depend on the total water fraction.

The change in the atmospheric escape is the smallest for the outermost planet b, which also has the smallest water fraction in the atmosphere according to the structure models. For better clarity, we include in Table 5 both the escape rate (i.e. the number of particles escaping per unit time) and the mass loss rate (i.e. mass escaping per unit time). Thus, for planet b, the escape rate reduces with the inclusion of water by a factor of 4.72. However, due to the increasing fraction of massive particles (mainly oxygen atoms) in the escaping material, the mass loss rate decreases by about a factor of two, which can be considered negligible from the point of view of atmospheric evolution (e.g., see the discussion in Kubyshkina et al. 2024).

For the compact atmosphere of planet d, despite the outflow parameters being very similar to those of planet b in the case of H/He atmospheres, the inclusion of water leads to significant changes. Namely, the escape rate drops by about 30 times, and the mass loss rate decreases by a factor of 5.3, which can effectively cease the atmospheric loss. For the innermost planet c, the water mass fraction for the $H_2O$ atmosphere predicted by internal structure models is almost equivalent to that of planet d, and their masses and radii are also similar. However, due to the higher temperature and XUV flux at the orbit of planet c, the photodissociation of water in its upper atmosphere becomes considerably more effective. This implies that despite a large water reservoir in the lower atmosphere, the water molecule
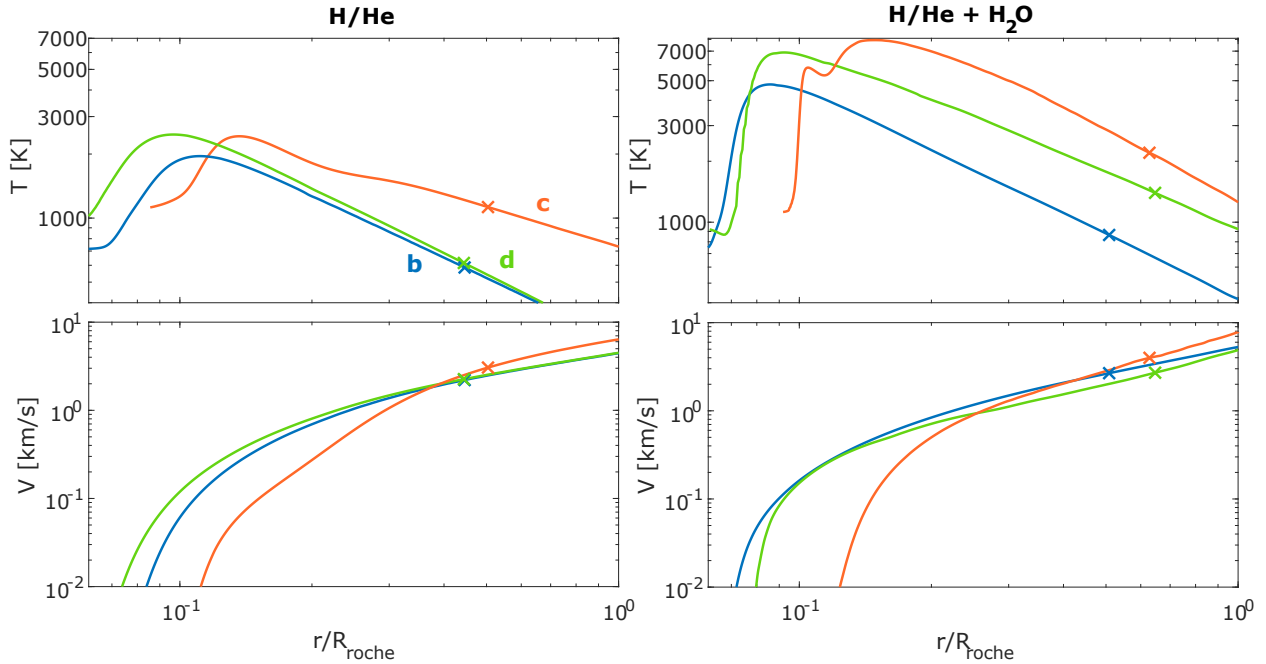
**Fig. 9.** Atmospheric temperature (left $Y$-axis, solid lines) and bulk outflow velocity (right $Y$-axis, dashed lines) against radial distance normalised to the Roche radii of the planets, as predicted by CHAIN models. The top panel shows results for the H/He atmospheres and the bottom panel for $H_2O$ atmospheres. The different colours correspond to planets b (blue), c (orange), and d (green). The crosses denote the positions of sonic points.

fraction in the region where photoionisation heating occurs remains minor relative to hydrogen and helium (maximum $H_2O/H^0$ number fraction is comparable to that of planet b and roughly 80 times lower than for planet d). In contrast, fractions of ions are ~3 times higher than for planet d. Thus, water molecule cooling becomes less effective; meanwhile, the number density of atomic oxygen released from water molecules in photodissociation reactions increases and the radiative oxygen line cooling, acting at higher altitudes, becomes gradually more prominent with increasing atmospheric temperature (see the dark-yellow dotted line in Figure 10). Therefore, despite the lesser number of water molecules in the upper atmosphere, the reduction in the escape becomes more significant for planet c than in the case of planet d (about a factor of 35 for the escape rate and a factor of about 6.5 for the mass loss rate).

## 5.3. Cooling rates

We show the dominant (radiative) cooling processes in the $H_2O$ atmospheres of planets b, c, and d in Figure 10. Molecular ($H_2O$) cooling contributes up to 10% of the total cooling in the lowermost atmospheric layers of planet c, and up to 43% and 27% for planets b and d, respectively. At higher altitudes, near the maximum of the photoionisation heating (the second peak of $H_{tot}$), the cooling is dominated by the line cooling of H and O, bremsstrahlung cooling (deceleration of free electrons due to the electromagnetic interaction with H ions, also known as free-free H radiation), production of $H^-$, and recombination of $H_2^+$, similarly to the H/He case. For planet c, the hottest in the system, other metal lines also contribute considerably in this region. Despite the input from individual lines being not that high, their joint contribution dominates the cooling between ~1.06–1.22 $R_{pl}$; the largest input, exceeding 10% of the total cooling rate each, comes from magnesium and calcium lines. The thorough testing of our models shows that the exact

picture of the heating/cooling processes acting in the atmospheric region below the 1 μbar level (shown by the black dotted line in Figure 10) depends strongly on a range of factors including the chosen lower boundary conditions and the shape of the SED employed in the simulations (in particular, the visible and infrared wavelengths), while the processes at the higher altitudes show a negligible dependence on these factors. However, we also find that the changes in heating/cooling rates in the densest atmospheric parts have a limited effect on the atmospheric loss rates; therefore, comparing the H/He and $H_2O$ atmospheres remains valid as long as one keeps the boundary and model parameters consistent for different atmospheric compositions.

## 5.4. Abundances of different atmospheric constituents

In addition to the differences in the total atmospheric loss rates and temperatures, the H/He and $H_2O$ models differ significantly in terms of the species that are being lost. We show the height abundances of different atmospheric constituents in $H_2O$ models in Figure 11, and summarise the number and mass fractions of different atoms and ions in the escaping material (taken at the sonic point) for all models in Table 6. We note that the total fraction of specific elements (sum of free neutral atoms, ions, and constituents of different molecules) at all altitudes is fixed due to our model assumptions (see above) and a more accurate treatment requires a multi-fluid approach (e.g. Schulik & Booth 2023). However, the ion/molecule fractions are defined with a detailed chemistry framework.

For all three planets, the abundance of water molecules in $H_2O$ models maximises at low altitudes and drops steeply with increasing height, thus their fraction above ~1.5 $R_{pl}$ becomes negligible. The same holds for $H_2$, OH, and CO molecules. It is notable that in the H/He atmospheres, $H_2$ is the most common hydrogen species below the μbar level, while in the $H_2O$ atmospheres most of the $H_2$ is bound in water molecules. The same
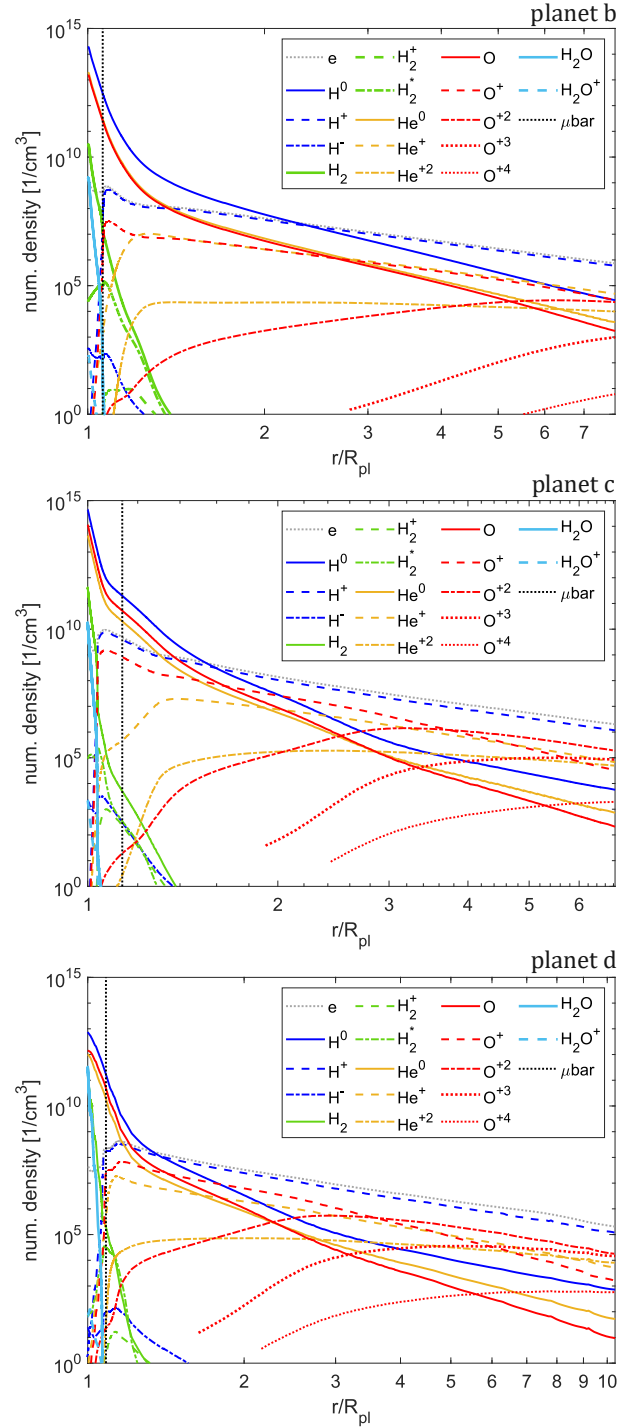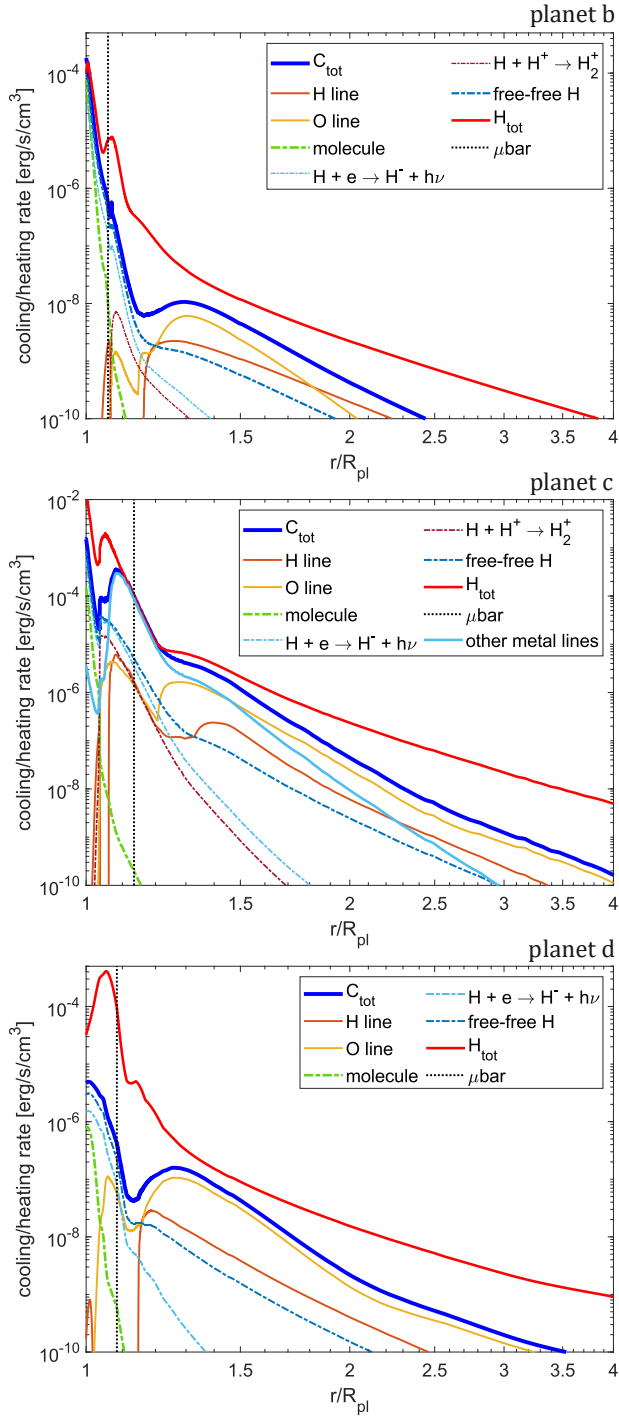
**Fig. 10.** Radiative cooling and heating rates against radial distance for the CHAIN runs of the $H_2O$ atmospheres of planets b (top panel), c (middle panel), and d (bottom panel). The rates are shown between 1 and 4 $R_{pl}$, where most of the photochemistry takes place; higher altitudes are dominated by adiabatic expansion. For individual cooling processes, we only show those that contribute at least 5% to the total cooling rates (at some specific altitude). The line styles are explained in the legends, where the notation is the following: $C_{tot}$ – total cooling rate (the sum of all radiative processes); $H_{tot}$ – total heating rate; μbar – the altitude corresponding to 1 μbar pressure level; X line – line cooling of the X element; molecule – the sum of molecule cooling processes (dominated by $H_2O$ molecule cooling); free-free H – bremsstrahlung cooling from hydrogen and helium.

**Fig. 11.** Numerical densities of relevant elements against the radial distance from the CHAIN runs of the $H_2O$ atmospheres of planets b, c, and d. The different line styles correspond to different species, as explained in the legend. The ΣH entry corresponds to the summed density of all hydrogen species (H, $H^+$, $H^-$, $H_2$, $H_2^+$, $H_2^*$, and $H_3^+$).

occurs for $H_2^+$. $H_2^+$, in turn, is necessary for the formation of $H_3^+$, which is therefore not present in $H_2O$ atmospheres in significant amounts. Thus, at higher altitudes, the inclusion of water leads to an increase in abundance of neutral and ionised oxygen, and in the region where the atmospheric material can be considered

**Table 6.** Elemental fractions at the sonic point for planets HIP 29442 b, HIP 29442 c, and HIP 29442 d predicted by CHAIN.

| Planet | Model | $H^0$ (%) | $H^+$ (%) | $He^0$ (%) | $He^+$ (%) | $He^{+2}$ (%) | $O^0$ (%) | $O^+$ (%) | $O^{+2}$ (%) |
|---|---|---|---|---|---|---|---|---|---|
| b | H/He | 31.02/24.30 | 59.80/46.86 | 2.78/8.65 | 6.08/18.92 | 0.23/0.71 | 0.02/0.24 | 0.02/0.30 | $7.4 \times 10^{-4}$/0.01 |
| b | $H_2O$ | 2.92/1.22 | 80.81/33.89 | 0.38/0.64 | 6.34/10.57 | 1.64/2.74 | 0.17/1.11 | 3.44/23.10 | 3.98/26.72 |
| c | H/He | 54.67/42.84 | 36.15/28.32 | 5.03/15.67 | 3.99/12.42 | 0.06/0.19 | 0.03/0.38 | 0.01/0.18 | $5 \times 10^{-5}$/$6 \times 10^{-4}$ |
| c | $H_2O$ | 0.37/0.11 | 73.03/22.20 | 0.05/0.06 | 4.33/5.23 | 2.96/3.58 | 0.01/0.07 | 2.17/10.55 | 11.97/58.20 |
| d | H/He | 19.71/15.44 | 71.11/55.72 | 1.75/5.46 | 6.84/21.28 | 0.49/1.53 | 0.01/0.15 | 0.03/0.37 | 0.003/0.04 |
| d | $H_2O$ | 0.44/0.15 | 72.95/24.70 | 0.03/0.04 | 3.26/4.39 | 4.05/5.44 | 0.01/0.05 | 1.36/7.38 | 10.68/57.84 |

**Notes.** The fractions of the elements are given in the format (number fraction)/(mass fraction). Note, that the total abundances of each element (neutral atoms and ions together) were set based on the interior models and do not vary with altitude; the ion/neutral and atom/molecule fractions are set by the chemical framework.

escaped (as such we take the sonic point), the outflow consists mainly of hydrogen, helium, and oxygen ions. The fraction of neutral oxygen and helium atoms remains small in all cases. For oxygen, the number fraction at the sonic point constitutes 0.02–0.13%, and the mass fraction 0.05–0.85%, highest for planet b; for neutral helium, the number and mass fractions in $H_2O$ atmospheres vary between 0.03–0.32% and 0.03–0.54%, respectively, while for H/He atmospheres these ranges are 1.24–5.03% and 3.85–15.67%. The mass fraction of $He^+$ in the outflow varies between 2.97–24.03% in all models, being higher for H/He models, while that of $He^{+2}$ is 0.19–3.64%, being higher for $H_2O$ atmospheres (in particular for hotter planets). The fraction of oxygen ions ($O^+$ and $O^{+2}$) at the sonic point in $H_2O$ models dominates over $H^+$ in terms of mass, though not number, and $O^{+2}$ ions constitute more than half of all oxygen ions at the sonic point for the two inner planets. Finally, though not included in Table 6, the fraction of $O^{+3}$ ions is non-negligible for the two inner planets (mass fractions of 2.9% and 4.5% for planets c and d, respectively), and fractions of $O^{+4}$ and $O^{+5}$ are non-zero.

Another result, potentially interesting for observations, is that the total fraction of neutral atoms at the sonic point and, in general, at high altitudes (where the escape can be probed in e.g. Ly$\alpha$) is significantly higher in H/He atmospheres (by a factor of ~7–64, increasing with equilibrium temperature). For 99% water atmospheres, the number fraction of $H^0$ in the escaping material is less than 1%, while most of the escaping hydrogen is ionised. This happens due to the increasing mean molecular weight of the atmosphere, making the gradients in density/pressure height profiles steeper, in particular at low altitudes, and, therefore, the ionisation front becomes narrower, though the ion fraction integrated over the whole simulation domain does not change as much. This can result in a decrease in the detectability of the escape in hydrogen/helium lines for the water-rich atmospheres compared to the pure hydrogen-helium atmospheres, even if the actual atmospheric mass loss rates are similar. This might lead to the non-detection of the atmospheric escape for some planets even if the theoretically predicted mass loss rates are high. We note, however, that the simulations presented above were performed employing the model configuration not including the adiabatic wind effect into the advection term within Cloudy runs (which is still the experimental part of Cloudy framework and therefore is not included in the 'default' configuration of CHAIN, though it is physically relevant; see a detailed discussion in Kubyshkina et al. 2024). The inclusion of this feature can lead to an increase of the fraction of neutral atoms in the outflow of up to a factor of a few, in particular for planet b with a puffier atmosphere. However, the outflow would remain ion-dominated.

# 6. Possible formation and evolution pathways

To discuss possible formation and evolution pathways of the HIP 29442 system, we compare the observed three-planet system to synthetic planetary systems generated using the Bern model (Alibert et al. 2005; Mordasini et al. 2009; Emsenhuber et al. 2021a,b), a coupled formation and evolution model. In the following, we use a variation of the nominal population of the New Generation Planetary Population Synthesis (NGPPS; Emsenhuber et al. 2021a,b) for solar mass stars with a formation phase extended from 20 to 100 Myr (Emsenhuber et al. 2023) and an improved evolution model (Burn et al. 2024). Each of the 1000 generated systems is given a system ID as an identifier and starts with 100 randomly distributed lunar-mass planetary embryos. Meanwhile, the initial conditions for the protoplanetary disks are sampled from observationally informed distributions using a Monte Carlo approach.

During the formation phase, the accretion of planetesimals and gas by these embryos is modelled along with the evolution of the gas disk, dynamical interactions between the embryos and their gas disk driven orbital migration. The long-term evolution of each planet is then modelled individually until an age of 5 Gyr, including atmospheric photoevaporation of both water and H/He, migration due to stellar tides and the cooling and contraction of the planetary interior. For the internal structure, it is assumed that the accreted water is uniformly mixed with any present H/He once the evolution phase of the model is reached.

Currently not yet included in this population are more recently studied effects such as hybrid pebble and planetesimal accretion (Kessler & Alibert 2023; Alibert et al. 2018), the dynamic formation of planetesimals and planetary embryos from dust and pebbles (Voelkel et al. 2020, 2021), planetesimal fragmentation (Kaufmann & Alibert 2023), MHD-wind driven disk evolution (Weder et al. 2023), the influence of structured disks (Lau et al. 2022; Jiang & Ormel 2023) and a description of orbital migration based on torque densities (Schib et al. 2022).

To identify possible formation and evolution pathways of HIP 29442, we now search this population for synthetic analogues of the observed system, thereby following a similar approach as Ulmer-Moll et al. (2023).

## 6.1. Finding analogues for the HIP 29442 system in the synthetic Bern model population

To define how close a synthetic planet is to one of the observed planets, we choose the logarithmic distance in the semi-major axis versus mass plane as our metric, analogous to
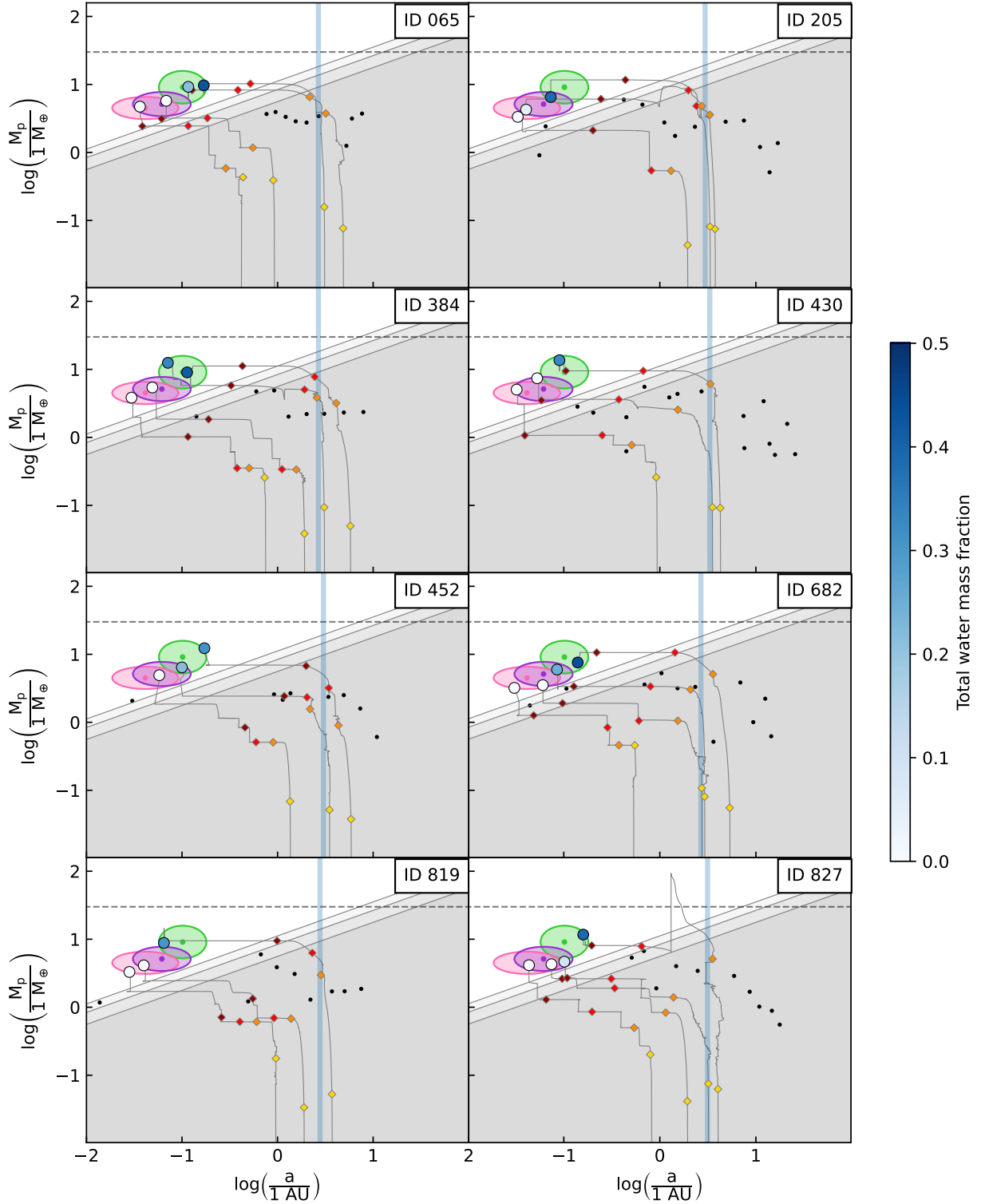
**Fig. 12.** Planetary mass vs semi-major axis plots of eight synthetic planetary system analogues for the observed HIP 29442 system (one per panel, with the Bern model system ID indicated in the upper right corner). These planetary system analogues are taken from the nominal NGPPS population (Emsenhuber et al. 2021a,b) for solar mass stars with an extended formation phase (Emsenhuber et al. 2023) and an improved evolution model (Burn et al. 2024). The green, pink and purple ellipses show the observational values for planets b, c, and d respectively, with a 25% tolerance in log that was used when identifying synthetic analogues for each planet. The areas shaded in grey show simple RV biases of 0.50, 0.75 and 1.00 m/s respectively. Synthetic planets below the 1 m/s RV bias are likely not observable and are shown as black dots, down to a mass of 0.5 $M_\oplus$. For the synthetic planets above an RV bias of 1 m/s, which form the part of the planetary system that could be observed, the planet's total water mass fraction is indicated by the marker colour, while the formation tracks are shown as black lines. For each formation track, the temporal evolution is indicated by diamond-shaped markers, which show the position of the planet at 0.1 Myr (yellow), 1 Myr (orange), 2 Myr (red) and 3 Myr (dark red). The vertical light blue line indicates the location of the water ice line of each synthetic system, which is assumed to be constant. The dashed black line indicates a mass of 30 $M_\oplus$, corresponding to the upper limit for the critical core mass given by Bodenheimer & Pollack (1986).
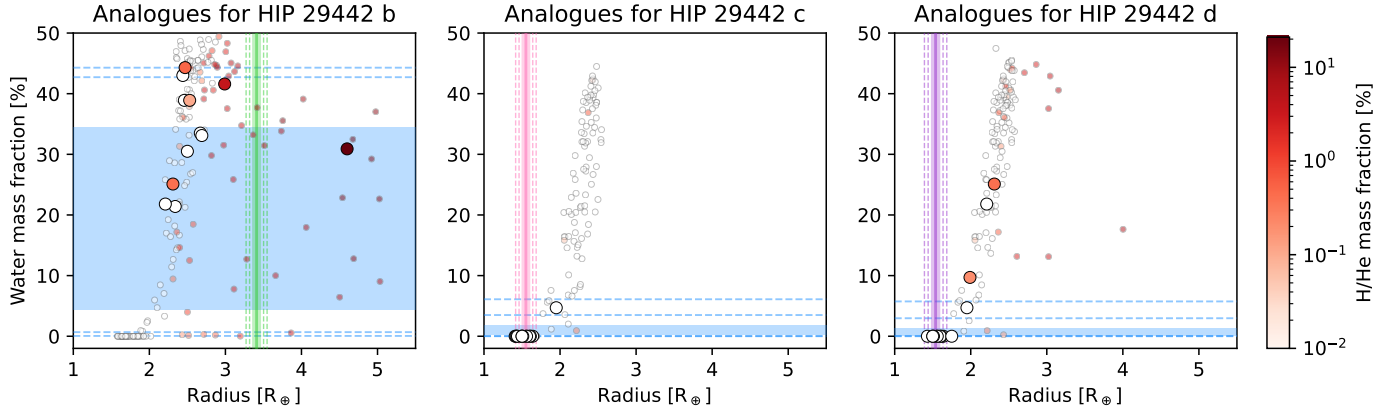
**Fig. 13.** Water mass fraction vs planet radius. The markers are colour-coded according to the H/He mass fraction for the synthetic analogues of HIP 29442 b, c, and d. The large points are the synthetic analogues of planet b, c, and d considering the full planetary system, while the transparent, smaller points in the background are the synthetic analogues for the single-planet system of each planet. The areas shaded in green, pink and purple respectively indicate the $1\sigma$ confidence interval of the observational radius for each planet, while the areas shaded in blue are the water mass fractions inferred from the internal structure modelling (model A1 with stellar Si/Mg/Fe prior and assuming a formation outside the iceline). The dashed lines indicate the $2\sigma$ and $3\sigma$ values of the respective distributions. Synthetic planets that fall in the shaded areas are good synthetic matches for the observed planets.

Kaufmann & Alibert (2023). Using this metric, we then define that a synthetic planet qualifies as an analogue for one of the observed planets if it lies in an elliptical area in the semi-major axis versus mass space with vertices and co-vertices at a 25% variation in log of the semi-major axis and mass of the observed planet. As the size of the synthetic population is limited to 1000 systems, the dimensions of these elliptical areas were chosen rather liberally and they do overlap for the three HIP 29442 planets, meaning that in some cases a single synthetic planet can be an analogue for two of the observed planets at once. We now select synthetic systems with at least one analogue for each of the observed planets. From this subset of the synthetic population we eliminate systems that, after applying a simple RV bias of 1 m/s, contain less than two or more than four observable planets, systems where one or more of these observable planets are giants ($M_\mathrm{p} > 30\ M_\oplus$), and also systems where the order of the synthetic planets does not match the observed system, due to the overlap of the elliptical areas used to identify synthetic analogues for the observed planets. This leaves us with the eight synthetic systems pictured in Figure 12.

In addition, we also identify analogues for each of the three observed planets separately, which we will in the following refer to as synthetic single-planet analogues. This allows us to make comparisons later on in this analysis between the planets of a certain kind present in the NGPPS population in general and the ones in systems like HIP 29442. We find in total 200 synthetic single-planet analogues for planet b, 227 for planet c and 238 for planet d.

Figure 13 summarises the radii, water and H/He mass fractions of the analogues for each of the three observed planets. Synthetic planets that fall in the areas shaded in colour are good synthetic matches for the observed planets with respect to their radii and water mass fractions inferred in Section 4. The radii of the synthetic planets (both for the system analogues and the single-planet analogues) generally fit reasonably well with the ones derived in Section 3 for HIP 29442 c and d, with some outliers with clearly larger radii especially for planet d. These outliers tend to have water mass fractions larger than a few percent and are from the higher end of the defined mass range where a synthetic planet counts as an analogue for the observed planet.

In contrast to planets c and d, planet b's observed radius lies more than 3 standard deviations above the average value for its synthetic system analogues. One possible explanation for this is the location of HIP 29442 b above the radius cliff, which also naturally emerges in the synthetic population (Burn et al. 2024) and means that the occurance rate of planets with radii above 3 $R_\oplus$ is much smaller than the one of planets between 2–3 $R_\oplus$. To find exact analogues of the HIP 29442 system, we would therefore likely need a larger synthetic population. This is to some extent confirmed when we also look at the single-planet analogues for HIP 29442 b (small dots in Figure 13), as most of these synthetic planets have radii below 3 $R_\oplus$. However, there are also other possible explanations, for instance that the NGPPS population was generated for a fixed stellar mass of 1 $M_\odot$, which is slightly higher than the value we derived for HIP 29442 in Section 2. It is also possible that the H/He loss rate in the synthetic population is currently too high and the synthetic planets therefore are too small and have a H/He mass fraction that is too low. This of course would then also affect the single-planet analogues. We did compare the present-day mass loss rates obtained in the previous section (see Table 5) to the ones for the synthetic planets at an age of 5 Gyr, and found values of the same orders of magnitude. However, this does not exclude differences in the mass loss rates earlier in the stellar evolution, when the evaporation is much stronger.

A large majority of the synthetic analogues of HIP 29442 c and d have lost their entire H/He envelope through photoevaporation. They also mostly do not contain any or only a small amount of water, up to a few percent in mass, with the exception of a few analogues for HIP 29442 d as discussed above. This is compatible with our results from Section 4, where we find envelope mass fractions of a few percent for a formation scenario outside the iceline with a very high envelope water mass fraction and very small envelope mass fractions of the order of $\sim 10^{-6}$ for a water-poor formation. In the latter case, these envelopes would likely have been lost during the planet's evolution. The full system analogues of HIP 29442 b have also lost most if not all accreted H/He, with only two synthetic planets that have a mass fraction of more than 1% of H/He. However, they all showcase water mass fractions between 20 and 45%. Compared to the results
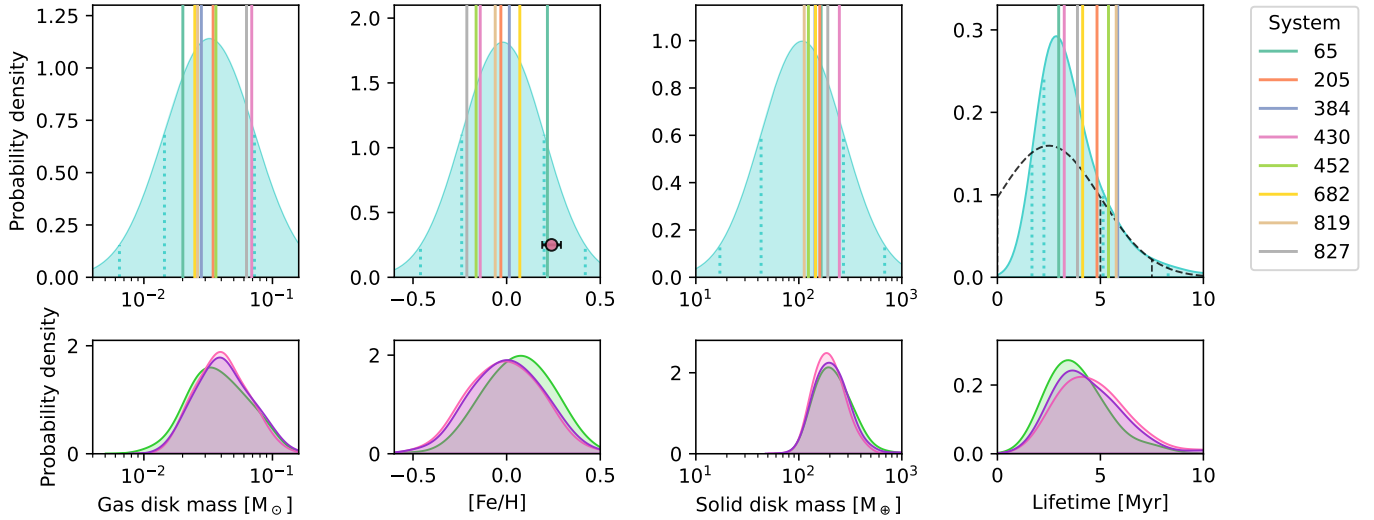
**Fig. 14.** Properties of the protoplanetary disks of the synthetic system analogues for the HIP 29442 system (coloured lines) compared to the distributions they were sampled from (turquoise curves, as specified by Emsenhuber et al. 2021b). The dotted lines show the one- and two-sigma error intervals of the plotted distributions. The bottom row shows the distributions of the same disk properties for the single-planet analogues for planets b (green), c (pink), and d (purple). Left: initial values of the gas disk masses with a probability density function fitted to Tychoniec et al. (2018). Middle left: disk metallicities indicative of the disks' dust-to-gas ratios, sampled from Santos et al. (2005). The red point indicates the observationally derived metallicity of HIP 29442. Middle right: initial values of the solid disk masses, calculated from the sampled gas disk masses and dust-to-gas ratios and compared to the initial solid disk masses of all systems in the synthetic NGPPS population. Right: disk lifetimes of the synthetic system analogues compared to the distribution of lifetimes calculated from the fraction of observed stars with disks at each age (Mamajek 2009, black curve) and the lifetimes of disks in the synthetic NGPPS population (turquoise).

from our internal structure analysis for a water-rich formation, the synthetic planets seem to have higher water mass fractions than what our internal structure analysis predicts, while at the same time more H/He seems to have been lost. This is in agreement with the scenario presented above of a H/He loss rate that is too high in the synthetic population, which could also explain lower planetary radii for the HIP 29442 b analogues. Another possibility is that the evaporation of water is underestimated in the Bern model. It is also possible that some of the water would in reality be stored in the interior of the planets (e.g. Dorn & Lichtenberg 2021), which makes it more difficult to compare the water mass fractions for the synthetic Bern model planets with the ones derived in Section 4. As is discussed further in Section 7, the reason for this is that the water mass fractions that are inferred by plaNETic do not refer to the total water content of each planet, but only to the water that is not dissolved in the mantle and core.

### 6.2. Patterns in the formation pathways of the Bern model analogues

Looking at the formation tracks of these eight synthetic systems as plotted in Figure 12, all of them would be classified as hybrids of classes I (compositionally ordered Earth and ice world systems) and II (migrated sub-Neptune systems) according to the system architecture classifications introduced in Emsenhuber et al. (2023). The corresponding analogues for HIP 29442 b form at a distance between 3 and 6 AU from their host star outside the iceline. Through the accretion of planetesimals, they grow to a mass of around 5-10 $M_\oplus$. At this point, they start migrating inwards while still accreting mass. Once they reach the equality mass or the saturation mass (the mass scales where migration becomes dominant over accretion; see Emsenhuber et al. 2023), they keep migrating inwards at constant mass and never reach

the critical core mass needed for rapid gas accretion. One exception is the analogue for planet b in system 827, which does reach the critical core mass, subsequently undergoes rapid gas accretion and reaches a mass of almost 100 $M_\oplus$, but then loses its envelope through a giant impact. This is in agreement with the findings of Venturini et al. (2020a), who also predict based on a pebble-based formation model that a planet with a mass and radius similar to HIP 29442 b should have formed beyond the iceline and be water-rich.

The formation tracks of the analogues for HIP 29442 c and d are a bit more diverse. Most of them initially form inside the iceline, at a distance between 0.4 and 2 AU, while some analogues for planet d also initially form just outside the iceline at around 3 or 4 AU. As is also outlined in Emsenhuber et al. (2023) for planets in class I systems, these planets first grow in-situ through the accretion of planetesimals until they reach the planetesimal isolation mass. While only the more massive planets outside the iceline reach a mass high enough for significant inward migration, the inner planets are caught in resonant chains and pushed inwards. As all planetesimals inside the iceline have been accreted at this point, solid growth is no longer possible and the planets migrate inwards at constant mass. Once the gas disk disperses, the planets start to undergo collisions and can grow further through giant impacts.

### 6.3. Common properties of the synthetic protoplanetary disks

As a next step, we study the initial conditions of the protoplanetary disks of the eight synthetic system analogues, as visualised in the upper panel of Figure 14, and compare them to the distributions they were sampled from (see Emsenhuber et al. 2021b for details on the chosen initial conditions of the population synthesis) and to the distributions of the corresponding disk properties of the single-planet analogues (lower panel in Figure 14).

Most of the synthetic disks have initial gas disk masses between 0.020 and 0.036 $M_\odot$, while two of the systems have slightly more massive initial gas disks at 0.063 and 0.069 $M_\odot$. When comparing this to the probability density function fitted to the histogram of class I disks reported by Tychoniec et al. (2018) from which the initial disk masses for the population were sampled, all values lie within one standard deviation from the mean and we do not see a clear pattern pointing towards high or low gas disk masses being required to form the system analogues of HIP 29442 (Figure 14, left). When looking at the distributions of the gas disk masses of the single-planet analogues for HIP 29442 b, c, and d, we can however see that disks with gas masses at the lower end of the initial distribution do not seem to be able to produce planets of these masses that end up on such close-in orbits.

We now investigate the dust-to-gas ratios of the synthetic disks. For the model population, the relevant parameter that is sampled is the disk metallicity, which is assumed to match the one of the star exactly. The dust-to-gas ratio is then calculated as $\frac{f_{D/G}}{f_{D/G,\odot}} = 10^{[Fe/H]}$, with $f_{D/G,\odot} = 0.0149$ (Lodders 2003). The stellar metallicities, in turn, are sampled from the distribution of Santos et al. (2005) for the Coralie RV search sample. When we now look at the metallicities of the eight disks of our analogue systems (Figure 14, middle left), all but one are within one standard deviation of the mean of this distribution, and the one outside (system 65) is just above the one sigma upper bound. Emsenhuber et al. (2023) find a positive correlation between the occurrence of sub-Neptune planets and the stellar metallicity, in agreement with observational results for the *Kepler* planets from Petigura et al. (2018). Mulders et al. (2016) also find that hot exoplanets with orbital periods of less than 10 days are preferentially found around metal-rich stars. HIP 29442 is in fact a metal-rich star with a metallicity of [Fe/H]= 0.24 ± 0.05 (see Table 1), which is in line with these studies. However, when looking at the stellar metallicity values of the system analogues for HIP 29442, we do not find the same trend, which shows that a high stellar metallicity is not necessarily required to form a system like HIP 29442 in the synthetic population. However, the spectrally derived metallicity of HIP 29442 is compatible with the metallicity of system 65, but the metallicity values of all the other synthetic system analogues lie below the $3\sigma$ lower bound of the observed value for HIP 29442. In principle, we should restrict the search for planetary system analogues to initial conditions that also fit the observed stellar metallicity. However, this would require a larger synthetic population. We also note that the distribution of the metallicity values of the disks of the synthetic single-planet analogues of planet b is shifted slightly towards higher metallicity values compared the single-planet analogues for planets c and d.

While the initial mass of the solid disk is not a Monte Carlo variable in the population synthesis but is instead calculated as the product of the sampled gas disk mass and dust-to-gas ratio, it is one of the most relevant parameters for determining the type of planetary system formed by a disk (Emsenhuber et al. 2023). As shown in the middle right panel of Figure 14, the solid disk masses of the eight system analogues of HIP 29442 all lie above the mean when compared to the entire NGPPS population, but within one sigma of the distribution. This is in agreement with the findings of Emsenhuber et al. (2023), who find that lower mass protoplanetary disks will not lead to the formation of sub-Neptunes, while disks with masses higher than this will likely lead to the formation of giant planets. We also see this when looking at the disks of the single-planet analogues, which all have solid disk masses of at least 50 $M_\oplus$.

For the lifetimes of the synthetic protoplanetary disks, the relevant parameter that is sampled as part of the population synthesis in the Bern model is the external photoevaporation rate, in combination with the initial disk mass. The photoevaporation rate is sampled from an empirical distribution that leads to lifetimes of the synthetic disks that match the lifetimes of observed disks, with a mean value between 3 and 4 Myr. The right panel of Figure 14 shows both the disk lifetimes derived from an exponential fit of observational data for the fraction of stars with disks at different ages (Mamajek 2009) and the distribution of the disk lifetimes of the systems in the NGPPS population. When comparing these distributions to the lifetimes of the eight synthetic disks in our sample, there seems to be a tentative trend towards disks with longer lifetimes that are needed to form a system like HIP 29442. The lifetimes of all eight synthetic disks lie above the mean value of Mamajek (2009), with three of them also lying above the $1\sigma$ upper bound. Also this correlation aligns with the conclusions drawn by Emsenhuber et al. (2023), who point out that disks with longer lifetimes are more likely to form systems containing migrated sub-Neptunes as the planets outside the ice-line then have more time to reach a mass of about 10 $M_\oplus$ and migrate inwards before the gas disk disperses.

### 6.4. Resonances

The upper panel of Figure 15 shows the position of the triplet of HIP 29442 and the selected NGPPS systems with respect to the web of mean motion resonances (MMRs). We denote $P_n$ as the orbital period of the $n^{th}$ planet in the chain, counting from the innermost planet to the outermost. The two-planet MMRs of the form $P_{n+1}/P_n = (k+q)/k$ (with $k$ and $q$ integers) are shown in purple, with $q = 1$ for continuous lines and $q = 2$ for dashed lines, the $P_{n+2}/P_n = 2$ resonance is shown in red. Black lines show three-body MMRs of the form $k/P_n - (k+q)/P_{n+1} + q/P_{n+2} = 0$ with $k$ and $q$ integers in the 1 to 6 range. For architecture comparisons, the usage of three-body MMRs is generally preferred, as the two-planet MMR resonant state depends on the eccentricity of the planets, which is not always easily constrained in exoplanetary systems (Cerioni et al. 2022). The first result of this graph concerns the orbital spacing between the planets of each system: The NGPPS systems have a spacing comparable to HIP 29442, with most of the period ratios above the 3:2 two-planet MMR, which is the most common MMR in resonant chains (e.g. Lopez et al. 2019; Leleu et al. 2021; Luque et al. 2023). The lower panel shows the relative distance of each triplet with respect to the closest three-planet MMR, divided by the relative distance to the second-closest three-planet MMR. This rescaling is used in order to account for the areas of the resonant web that are more densely populated. One can see that HIP 29442, along with the NGPPS systems, are quite far from any three-body resonance when compared to systems that are known to be in resonant chains, such as TOI-178 and K2-138 (Lopez et al. 2019; Leleu et al. 2021; Delrez et al. 2023). If the HIP 29442 system initially formed as a resonant chain, it grew unstable during or after the protoplanetary disk phase (e.g. Izidoro et al. 2017).

### 6.5. Other architecture frameworks

As discussed above, Emsenhuber et al. (2023) classify the architecture of synthetic planetary systems based on the planetary formation tracks. There are also other works that study the architecture of planetary systems, most of which are based
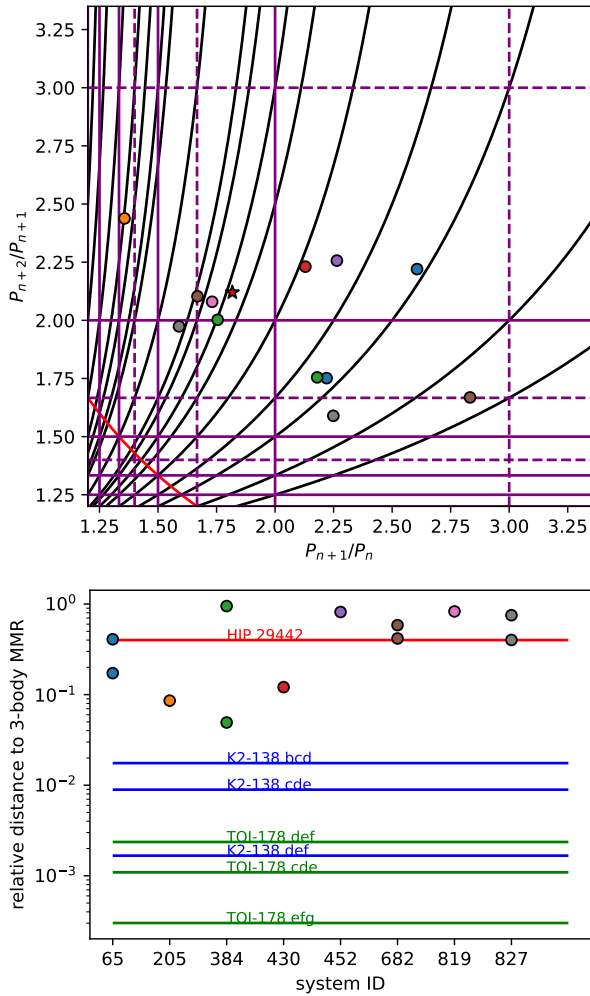
**Fig. 15.** Resonance behaviour of the observed HIP 29442 system and the synthetic system analogues. The top panel shows the HIP 29442 system (red star) with respect to the web of three-body MMRs (in black) and two-body MMRs (in purple and red). The coloured circles show the position of the triplets of the analogue systems from the synthetic NGPPS population, the system ID corresponding to each colour is given on the x-axis of the bottom panel. The bottom panel shows the same triplets with their relative distance to the nearest three-body MMR. The coloured lines show the distance to three-body MMRs for the observed systems HIP 29442, K2-138 and TOI-178.

on the directly observable, present-day properties of the planets in the system to be classified (e.g. Lissauer et al. 2011; Fabrycky et al. 2014; Millholland et al. 2017; Weiss et al. 2018; Mishra et al. 2023a,b; Davoult et al. 2024).

We now apply one of these architecture frameworks, the one from Davoult et al. (2024), to the HIP 29442 system. Their framework is based on the four architecture classes introduced in Mishra et al. (2023a,b), so each planetary system is classified as having a similar, mixed, ordered or anti-ordered architecture. Davoult et al. (2024) base their architecture classification on a Principal Component Analysis of the planetary systems with respect to the logarithmic distance of the planets from the star and the logarithmic masses of the planets. In this framework, HIP 29442 is a system of similar architecture, which is characterised by Davoult et al. (2024) as consisting of small planets, i.e. Earth-sized planets, super-Earths and sub-Neptunes. As the study points out, the formation of such systems has been investigated in detail by multiple authors, such

as Izidoro et al. (2017), Goldberg & Batygin (2022) and Batygin & Morbidelli (2023).

## 7. Discussion

### 7.1. Interior modelling sensitivity

In Section 4, we have modelled the internal structure of all three planets in the HIP 29442 system, using the planetary radii and masses derived in Section 3. For each planet, we consider that it could have formed inside the iceline, assuming that water was only accreted as part of the accreted gas, as well as a formation scenario outside the iceline, where we assume that the planet also accreted water in solid form. We find that the mean density of all three planets can be explained with either of the two assumptions. In the case of a formation scenario inside the iceline, we find that HIP 29442 b can be explained by an envelope mass fraction of a few percent, while the median values for the inferred envelope mass fractions for HIP 29442 c and d lie of the order of $10^{-6}$ and would almost certainly have been lost through evaporation. For all three planets, the water mass fractions in the envelope are, by construction, very low in this scenario. Instead, if we assume that the planets formed outside the iceline and also accreted water in solid form, we find a wide range of possible envelope mass fractions up to almost 60% for HIP 29442 b, with water mass fractions in the envelope of up to almost 90%. For HIP 29442 c and d, we find envelope mass fractions of a few percent in this scenario, with envelopes that are almost entirely made up of water. In Section 5, we then used a hydrodynamic modelling approach to study the influence of our inferred atmospheric compositions, both for a water-rich and water-poor formation scenario, on the conditions in the upper atmospheres of such planets and the expected atmospheric mass loss rates.

There are of course a number of limitations to this modelling approach. One aspect is that the calculated radius of a given planetary structure is still very model-dependent, especially for planets with larger envelope mass fractions. Haldemann et al. (2024) studied in detail how the use of updated EoS influences the calculated transit radius of a planetary structure, including a comparison of the forward model of BICEPS with the commonly used isocomposition curves from Zeng et al. (2019), and found differences of a few percent for predominantly rocky exoplanets and of 10% or larger for volatile-rich planets. Aguichine et al. (2021) present mass-radius relations for water-rich planets and find steam envelopes that are significantly larger compared to the transit radii calculated with BICEPS, with differences of up to ~20% for planets with small masses and high equilibrium temperatures. These differences can be caused by discrepancies in the chosen irradiation model, opacities and definition of the transit radius. This is also discussed by Venturini et al. (2024, their Section C.2), who point out that the key difference between BICEPS and the models of Aguichine et al. (2021) is that the latter assume the core-envelope boundary to be extremely hot based on evolution calculations accounting for the runaway greenhouse effect of water, an effect which more recent works point out might have been overestimated in the past (Selsis et al. 2023). Nixon & Madhusudhan (2021) also study planetary structures where the water and H/He components of the planet's atmosphere are not mixed and find significantly different radii for the two cases. This is an additional source of degeneracy that we do not consider in our inverse modelling. However, in this case also the runaway greenhouse effect needs to be considered, as hydrogen and supercritical water behave close to an ideal mixture

(Soubiran & Militzer 2015) and separate water and H/He layers would therefore not be stable under certain conditions (Turbet et al. 2019, 2020; Pierrehumbert 2023; Innes et al. 2023).

A second important aspect is that we do not currently consider the geophysical evolution of each planet in our model. Dorn & Lichtenberg (2021) show that large quantities of water can be stored in magma oceans of super-Earths and sub-Neptunes. Meanwhile, Vazan et al. (2022) study the interiors of ice-rich planets and find that ice and rock are expected to stay mixed even after billions of years of thermal evolution. In both cases, the water mass fractions inferred in Section 4 would not refer to the total water content of each planet, but to the amount of water not dissolved in the interior, as also pointed out by Haldemann et al. (2024). It is also possible that interactions between volatiles and a magma ocean produce additional, endogenic water (e.g. Kite et al. 2020), which makes the interpretation of a planet's water content even more complicated.

### 7.2. The HIP 29442 system in the context of the radius valley

As a next step, we explore how the HIP 29442 system fits in with two of the most popular explanations for the radius valley in the literature, on the one hand the loss of pure H/He envelopes either through photoevaporation (e.g. Owen & Wu 2017; Jin & Mordasini 2018) or core-powered mass loss (Ginzburg et al. 2018; Gupta & Schlichting 2019) and on the other hand a scenario in line with coupled planet formation and evolution models, which predict water-rich sub-Neptunes (Venturini et al. 2020a, 2024; Burn et al. 2024). For the first scenario, we note that the present-day accuracy and completeness of observations remains insufficient to distinguish between photoevaporation and core-powered mass loss (Rogers et al. 2021; Gupta et al. 2022). For both mechanisms, we therefore consider the framework from Kubyshkina & Fossati (2022), which is a coupled interior-hydrodynamic atmospheric escape model. The underlying atmospheric mass loss model of this framework reproduces both the photoevaporation and the core-powered mass loss regime and predicts radius valley parameters for both regimes (Affolter et al. 2023).

Using this framework, Kubyshkina & Fossati (2022) calculated model boundaries in the mass-radius space by combining a database of evolutionary tracks run up to 10 Gyr for planets with pure H/He envelopes with different masses, at different orbital separations and for 1 $M_\odot$ stars with different rotation histories. These boundaries then predict the expected radius spread of the exoplanet population. Figure 16 shows a mass-radius diagram with the observed planetary parameters for HIP 29442 c in the upper and HIP 29442 b and d in the lower panel, along with the model boundaries for the relevant temperature ranges corresponding to the equilibrium temperatures of the observed planets. Two different initial atmospheric mass fractions are considered for calculating the upper model boundaries (short and long dashed lines), based on the analytical fit from Mordasini (2020) ('basic setup') and assuming massive initial envelopes ('migrated scenario'), respectively. In both cases, the initial atmospheric mass fraction depends on the planetary mass and, in the case of the basic setup, also on the orbital separation (hence, temperature). Therefore, the whole range of initial atmospheric mass fractions of the models in Figure 16 ranges between 0.5–70% of the total planetary mass. For planets with parameters similar to the planets in the HIP 29442 system, they are ∼10% or ∼26% for planet b, ∼3% or ∼15% for planet c, and ∼5% or ∼17% for planet d, with the larger values in each case corresponding to the migrated scenario.
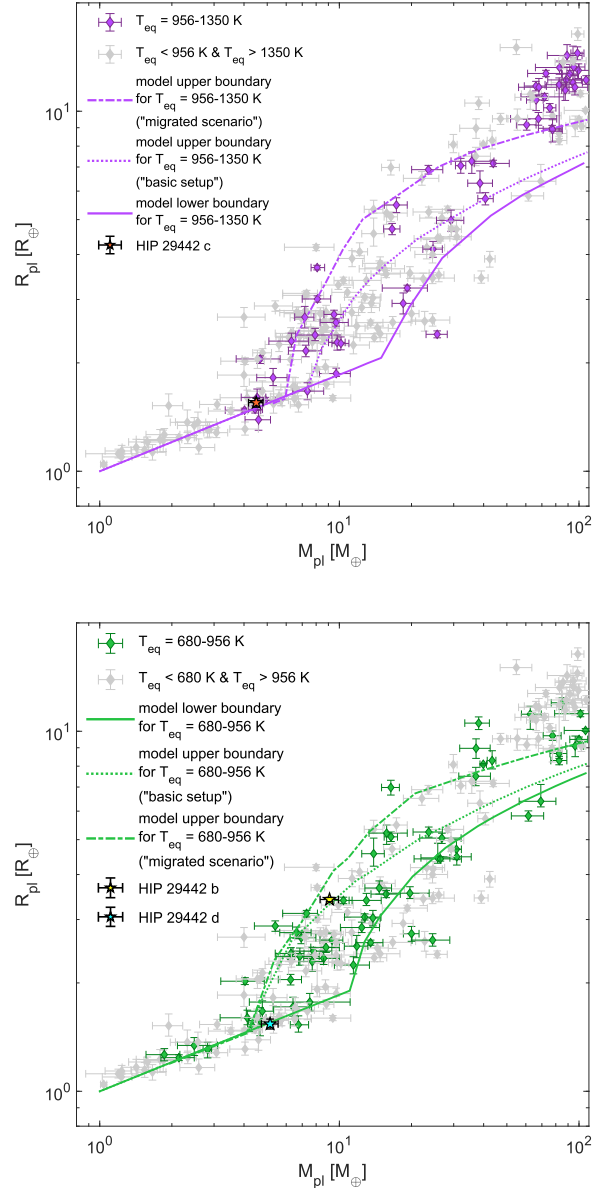
**Fig. 16.** Location of HIP 29442 c (upper panel) and HIP 29442 b and d (lower panel) in the mass radius diagram, in relation to the expected radius spread at an age of 5 Gyr according to Kubyshkina & Fossati (2022), who ran a database of evolutionary tracks for planets with pure H/He envelopes. The solid lines show the lower model boundary, the short dashed lines (labelled "basic setup" in the legend) the upper model boundary assuming initial H/He mass fractions calculated according to Mordasini (2020) and the long dashed lines (labelled "migrated scenario") assuming massive initial H/He mass fractions.

We can see that the H/He models predict HIP 29442 c to have lost any H/He envelope at an age of 5 Gyr independently of the size of its initial envelope and the rotation history of its host star. This is in agreement with the observed radius values and our internal structure modelling results for a prior consistent with a formation inside the iceline. HIP 29442 d, in turn, lays at the edge of the radius valley, among the planets that can keep or lose their atmospheres upon the initial parameters and the irradiation history (near the fork made by the boundary lines in Figure 16). Here, the upper model boundaries are given by the modelled planets at the lower edge of the temperature range and evolving around an inactive star, while the lower boundary

corresponds to the higher edge of the temperature range and an active host star. For the equilibrium temperature of planet d, the planet would, in fact, need a mass of ~6–7 $M_\oplus$ to keep a H/He envelope even around a slowly rotating star, which is ~5–30% higher than the mass we derived observationally. Meanwhile, HIP 29442 b lies close to the model upper boundary for initial H/He mass fractions calculated using Mordasini (2020) and therefore well within the expected radius spread. According to the evolution models by Kubyshkina & Fossati (2022), planets in this parameter range can lose ~45–80% of their initial H/He envelopes depending on their stellar rotation history, implying HIP 29442 b had to start with an atmospheric mass fraction of ~10–20% if we consider the results of our internal structure models for a formation scenario inside the iceline. The observed radii of the HIP 29442 system are therefore in agreement with the interpretation of the radius valley based on the hydrodynamic escape of H/He envelopes.

However, if we consider the analysis of possible formation and evolution tracks we conducted in Section 6, we do not find any synthetic planetary system analogues where the analogues for all three planets form inside the iceline. Of course, this depends on some fundamental assumptions underlying the model used to generate the synthetic population. Including different physical processes such as MHD-wind driven disks (where there could be less orbital migration than for the currently included turbulent disks) or pebble drift (which could bring a large amount of refractory solids into the interior part of the disk) could potentially allow to form the planets more or less in situ.

This brings us to the second scenario. In our analysis of possible formation and evolution tracks of the observed system, we identified a set of eight synthetic systems in the considered variation of the nominal NGPPS population that match the properties of the observed system well with respect to the masses and semimajor axes of the planets. From our tests, we found that the radii, water mass fractions, and H/He mass fractions of these synthetic planets match the ones derived in Sections 3 and 4 for the observed planets well for planets c and d, while the synthetic analogues for planet b have radii that are too low and water mass fractions that are slightly too high compared to the values for the observed planet. As we have pointed out, this could potentially be explained by an overestimated H/He and an underestimated water loss rate in the model. The higher water mass fractions could also be explained by some of the water being dissolved in the interior of the planet, as the water mass fractions we inferred as part of our internal structure analysis only consider the water stored in the envelope of the planet. Furthermore, we have also tested the resonance behaviour of the observed and the synthetic systems and found them to be similar in that they are all quite far from any 3-body resonance. When we consider these eight synthetic systems, all analogues for planet b formed beyond the iceline, while the analogues for planets c and d mostly formed inside the iceline with some that formed just outside it.

For the water-rich atmospheres inferred by our internal structure models using a prior consistent with a formation outside the iceline, a model for estimating the atmospheric loss self-consistently throughout the evolution does not currently exist. However, we can use the results obtained in Section 5 to make some preliminary estimates. For present-day parameters with the inclusion of water into H/He atmospheres, we get a reduction in the mass loss by about an order of magnitude for planets c and d and by about a factor two for planet b. This implies that HIP 29442 d, which already lies close to the borderline of evaporation for pure H/He atmospheres, would likely hold on to (some of) its atmosphere. In turn, HIP 29442 c could lose

~0.4–0.9 $M_\oplus$ of volatiles even in the case of water-rich atmospheres. This assumes the mass loss rates in the first Gyr of the evolution to be 10–30 times higher than at present, which takes into account higher XUV but ignores the possible planetary radius inflation at early ages. Finally, for HIP 29442 b, we can consider that H/He is more easily lost than water, which means that the atmospheric water mass fraction will only increase during evolution. The present-day value for the reduction in the escape rates between H/He and water-rich atmospheres is therefore an upper limit. This means that we can expect the primordial atmosphere of HIP 29442 b to be at least ~30% heavier than the present-day one. From these results we can therefore conclude that the observed properties of the HIP 29442 system are also in agreement with this second explanation for the bimodality of the radius distribution.

Overall, we have shown that the observationally derived parameters of the planets in the HIP 29442 system can be explained on the one hand by the classical evaporation scenario of pure H/He envelopes, either through photoevaporation or core-powered mass loss, but on the other hand also by the water-rich sub-Neptune scenario predicted by coupled formation and evolution models. While it is well established that most planetary systems straddling the radius valley can be explained using the photoevaporation model (e.g. Owen & Campos Estrada 2020), this has not been investigated systematically for the water-rich sub-Neptune hypothesis so far, which makes our findings especially interesting. Although it is not possible to clearly distinguish between the two scenarios based on the currently available observations, our analysis provides a strong case to search for water in the atmospheres of the planets in the HIP 29442 system with JWST.

## 8. Conclusions and summary

In this study we presented the results of an extensive photometric follow-up campaign with CHEOPS of the three planets transiting the evolved K0 star HIP 29442 on orbits of 3.5 days (planet c), 6.4 days (planet d), and 13.6 days (planet b). We obtained a total of 17 visits with a combined observing time of 9.6 days and containing 20 transits, which, together with the data from TESS sectors 6 and 33, allowed us to derive precise radii of $3.410 \pm 0.046$, $1.551 \pm 0.045$, and $1.538 \pm 0.049$ $R_\oplus$ for HIP 29442 b, c, and d respectively. These radii are compatible within $<1\sigma$ with the values previously derived by Damasso et al. (2023) for planets b and c, while for planet d, our value and error are $\sim3.4\sigma$ larger than their median value ($\sim1.5\sigma$ using their larger uncertainties). This changed the density of this middle planet from one compatible with a bare Mercury-like core to one that is approximately compatible with a bare Earth-like core instead, and led us to conclude that it is advisable to be cautious when determining the radii of small planets from multi-year TESS photometry when there are significant gaps between observations and the per-transit S/N is low. We also re-ran the RV model from Damasso et al. (2023) including not only their ESPRESSO RVs, but also additional public Keck-HIRES data from Akana Murphy et al. (2023). Our derived planetary masses of $9.10^{+0.82}_{-0.79}$, $4.50 \pm 0.32$, and $5.14 \pm 0.41$ $M_\oplus$ for HIP 29442 b, c, and d respectively are in good agreement with the values presented in Damasso et al. (2023). Overall, this makes HIP 29442 one of the most precisely characterised multiplanetary systems spanning the radius valley to date.

These very precise radii and masses then provided us with an ideal starting point for analysing the internal structure of the three planets and the formation history of the system, which is

especially interesting as HIP 29442 is a multiplanet system spanning the radius valley. For this purpose, we introduced a new version of our neural network-based Bayesian internal structure modelling framework (`plaNETic`), which is publically available. We found that the mean densities of all three planets can be explained using compositional priors informed by both a water-poor and a water-rich formation scenario. From our models, we expect HIP 29442 b to host a H/He dominated envelope of a few percent in mass with a very low envelope water mass fraction if it formed inside the iceline while in case of the planet forming outside the iceline, a wide range of compositions is possible, with envelope mass fractions ranging up to almost 60% and water mass fractions in the envelope of up to almost 90%. For HIP 29442 c and d, we found very low envelope mass fractions of the order of $10^{-6}$ that would almost certainly have evaporated in the water-poor formation scenario, and envelopes of up to a few percent in mass made up almost entirely of water for a water-rich formation outside the iceline. We therefore conclude that if planets c and d do have an envelope, it cannot be pure H/He, but needs to be of higher metallicity.

Further, we identified possible formation and evolution pathways of the system by identifying system analogues in the synthetic NGPPS population and found that according to the Bern model for planet formation and evolution, HIP 29442 b likely formed at a distance between 3 and 6 AU outside the iceline and then migrated inwards, while planets c and d likely formed inside or just barely outside the iceline. We also found that according to our analysis, a protoplanetary disk with a disk mass between 100 and 300 $M_\oplus$ and longer than average lifetime is necessary to form a system like HIP 29442.

Finally, we showed that the derived observational parameters of this system are compatible with both of the most popular explanations for the radius valley in the literature, sub-Neptunes with pure H/He envelopes undergoing atmospheric escape either through photoevaporation or core-powered mass loss, and a scenario with water-rich sub-Neptunes as predicted by planet formation and evolution models.

Software. The following software packages have been used for this publication: Python-numpy (Harris et al. 2020), Python-pandas (McKinney et al. 2010), Python-matplotlib (Hunter 2007), Python-seaborn (Waskom 2021), Python-tensorflow (Abadi et al. 2015), Python-scipy (Virtanen et al. 2020).

# References

Abadi, M., Agarwal, A., Barham, P., et al. 2015, TensorFlow: Large-Scale Machine Learning on Heterogeneous Systems, software available from https://www.tensorflow.org
Acuña, L., Deleuil, M., Mousis, O., et al. 2021, A&A, 647, A53
Acuña, L., Lopez, T. A., Morel, T., et al. 2022, A&A, 660, A102
Adibekyan, V., Dorn, C., Sousa, S. G., et al. 2021, Science, 374, 330
Aguichine, A., Mousis, O., Deleuil, M., & Marcq, E. 2021, ApJ, 914, 84
Affolter, L., Mordasini, C., Oza, A. V., Kubyshkina, D., & Fossati, L. 2023, A&A, 676, A119
Akana Murphy, J. M., Batalha, N. M., Scarsdale, N., et al. 2023, AJ, 166, 153
Alibert, Y., & Venturini, J. 2019, A&A, 626, A21
Alibert, Y., Mordasini, C., Benz, W., & Winisdoerffer, C. 2005, A&A, 434, 343
Alibert, Y., Venturini, J., Helled, R., et al. 2018, Nat. Astron., 2, 873
Batalha, N. M., Borucki, W. J., Bryson, S. T., et al. 2011, ApJ, 729, 27
Batygin, K., & Morbidelli, A. 2023, Nat. Astron., 7, 330
Baumeister, P., Padovan, S., Tosi, N., et al. 2020, ApJ, 889, 42
Benneke, B., Roy, P.-A., Coulombe, L.-P., et al. 2024, arXiv e-prints [arXiv:2403.03325]
Benz, W., Broeg, C., Fortier, A., et al. 2021, Exp. Astron., 51, 109
Bishop, C. M. 2006, Pattern Recognition and Machine Learning (Information Science and Statistics) (Berlin, Heidelberg: Springer-Verlag)
Blackwell, D. E., & Shallis, M. J. 1977, MNRAS, 180, 177
Bodenheimer, P., & Pollack, J. B. 1986, Icarus, 67, 391
Bonfanti, A., Ortolani, S., Piotto, G., & Nascimbeni, V. 2015, A&A, 575, A18
Bonfanti, A., Ortolani, S., & Nascimbeni, V. 2016, A&A, 585, A5
Bonfanti, A., Delrez, L., Hooton, M. J., et al. 2021, A&A, 646, A157
Bonfanti, A., Brady, M., Wilson, T. G., et al. 2024, A&A, 682, A66
Bonomo, A. S., Dumusque, X., Massa, A., et al. 2023, A&A, 677, A33
Brandeker, A., Patel, J. A., & Morris, B. M. 2024, PIPE: Extracting PSF photometry from CHEOPS data, Astrophysics Source Code Library [record ascl:2404.002]
Brugger, B., Mousis, O., Deleuil, M., & Deschamps, F. 2017, ApJ, 850, 93
Burn, R., Mordasini, C., Mishra, L., et al. 2024, Nat. Astron.
Carter, J. A., Agol, E., Chaplin, W. J., et al. 2012, Science, 337, 556
Castelli, F., & Kurucz, R. L. 2003, in IAU Symp., 210, Modelling of Stellar Atmospheres, eds. N. Piskunov, W. W. Weiss, & D. F. Gray, A20
Cerioni, M., Beaugé, C., & Gallardo, T. 2022, MNRAS, 513, 541
Chaturvedi, P., Bluhm, P., Nagel, E., et al. 2022, A&A, 666, A155
Claret, A. 2017, A&A, 600, A30
Claret, A. 2021, RNAAS, 5, 13
Cloutier, R., Eastman, J. D., Rodriguez, J. E., et al. 2020, AJ, 160, 3
Damasso, M., Rodrigues, J., Castro-González, A., et al. 2023, A&A, 679, A33
Davoult, J., Alibert, Y., & Mishra, L. 2024, A&A, in press, https://doi.org/10.1051/0004-6361/202449330
Delrez, L., Ehrenreich, D., Alibert, Y., et al. 2021, Nat. Astron., 5, 775
Delrez, L., Leleu, A., Brandeker, A., et al. 2023, A&A, 678, A200
Dorn, C., & Lichtenberg, T. 2021, ApJ, 922, L4
Dorn, C., Khan, A., Heng, K., et al. 2015, A&A, 577, A83
Dorn, C., Venturini, J., Khan, A., et al. 2017, A&A, 597, A37
Dorn, C., Mosegaard, K., Grimm, S. L., & Alibert, Y. 2018, ApJ, 865, 20
Ehrenreich, D., Delrez, L., Akinsanmi, B., et al. 2023, A&A, 671, A154
Emsenhuber, A., Mordasini, C., Burn, R., et al. 2021a, A&A, 656, A69
Emsenhuber, A., Mordasini, C., Burn, R., et al. 2021b, A&A, 656, A70
Emsenhuber, A., Mordasini, C., & Burn, R. 2023, Eur. Phys. J. Plus, 138, 181
Espinoza, N. 2018, RNAAS, 2, 209
Fabrycky, D. C., Lissauer, J. J., Ragozzine, D., et al. 2014, ApJ, 790, 146
Ferland, G. J., Chatzikos, M., Guzmán, F., et al. 2017, Rev. Mex. Astron. Astrofis., 53, 385
Foreman-Mackey, D., Luger, R., Agol, E., et al. 2021, J. Open Source Softw., 6, 3285
Fortier, A., Simon, A. E., Broeg, C., et al. 2024, A&A, 687, A302
Fortney, J. J., Mordasini, C., Nettelmann, N., et al. 2013, ApJ, 775, 80
France, K., Loyd, R. O. P., Youngblood, A., et al. 2016, ApJ, 820, 89
Freedman, R. S., Lustig-Yaeger, J., Fortney, J. J., et al. 2014, ApJS, 214, 25
Fressin, F., Torres, G., Désert, J.-M., et al. 2011, ApJS, 197, 5
Fulton, B. J., & Petigura, E. A. 2018, AJ, 156, 264
Fulton, B. J., Petigura, E. A., Howard, A. W., et al. 2017, AJ, 154, 109
Gaia Collaboration (Brown, A. G. A., et al.) 2021, A&A, 649, A1
Gaia Collaboration (Vallenari, A., et al.) 2023, A&A, 674, A1
Giacalone, S., Dressing, C. D., Jensen, E. L. N., et al. 2021, AJ, 161, 24
Ginzburg, S., Schlichting, H. E., & Sari, R. 2018, MNRAS, 476, 759
Goffo, E., Gandolfi, D., Egger, J. A., et al. 2023, ApJ, 955, L3
Goldberg, M., & Batygin, K. 2022, AJ, 163, 201
Goodfellow, I., Bengio, Y., & Courville, A. 2016, Deep Learning (MIT Press)
Guillot, T. 2010, A&A, 520, A27

Guimond, C. M., Wang, H., Seidler, F., et al. 2024, Rev. Mineral. Geochem., 90, 259
Gupta, A., & Schlichting, H. E. 2019, MNRAS, 487, 24
Gupta, A., Nicholson, L., & Schlichting, H. E. 2022, MNRAS, 516, 4585
Hakim, K., Rivoldini, A., Van Hoolst, T., et al. 2018, Icarus, 313, 61
Haldemann, J., Alibert, Y., Mordasini, C., & Benz, W. 2020, A&A, 643, A105
Haldemann, J., Ksoll, V., Walter, D., et al. 2023, A&A, 672, A180
Haldemann, J., Dorn, C., Venturini, J., Alibert, Y., & Benz, W. 2024, A&A, 681, A96
Harris, C. R., Millman, K. J., van der Walt, S. J., et al. 2020, Nature, 585, 357
Ho, C. S. K., & Van Eylen, V. 2023, MNRAS, 519, 4056
Holmberg, M., & Madhusudhan, N. 2024, A&A, 683, L2
Hooton, M., Adibekyan, V., Alibert, Y., et al. 2021, TOI-178: the best laboratory for testing planetary formation theories, JWST Proposal. Cycle 1, ID. #2319
Hunter, J. D. 2007, Comput. Sci. Eng., 9, 90
Innes, H., Tsai, S.-M., & Pierrehumbert, R. T. 2023, ApJ, 953, 168
Izidoro, A., Ogihara, M., Raymond, S. N., et al. 2017, MNRAS, 470, 1750
Izidoro, A., Schlichting, H. E., Isella, A., et al. 2022, ApJ, 939, L19
Jiang, H., & Ormel, C. W. 2023, MNRAS, 518, 3877
Jin, S., & Mordasini, C. 2018, ApJ, 853, 163
Jin, S., Mordasini, C., Parmentier, V., et al. 2014, ApJ, 795, 65
Johnstone, C. P., Bartel, M., & Güdel, M. 2021, A&A, 649, A96
Kaufmann, N., & Alibert, Y. 2023, A&A, 676, A46
Kessler, A., & Alibert, Y. 2023, A&A, 674, A144
Kingma, D., & Ba, J. 2015, in International Conference on Learning Representations (ICLR), San Diego, CA, USA
Kite, E. S., Fegley, Bruce, J., Schaefer, L., & Ford, E. B. 2019, ApJ, 887, L33
Kite, E. S., Fegley, Bruce, J., Schaefer, L., & Ford, E. B. 2020, ApJ, 891, 111
Kubyshkina, D., & Fossati, L. 2022, A&A, 668, A178
Kubyshkina, D., Fossati, L., Erkaev, N. V., et al. 2018, A&A, 619, A151
Kubyshkina, D., Fossati, L., & Erkaev, N. V. 2024, A&A, 684, A26
Kurucz, R. L. 1993, SYNTHE spectrum synthesis programs and line data (Cambridge, MA: Smithsonian Astrophysical Observatory)
Lacedelli, G., Wilson, T. G., Malavolta, L., et al. 2022, MNRAS, 511, 4551
Lau, T. C. H., Drążkowska, J., Stammler, S. M., Birnstiel, T., & Dullemond, C. P. 2022, A&A, 668, A170
Lee, E. J., & Chiang, E. 2016, ApJ, 817, 90
Leleu, A., Alibert, Y., Hara, N. C., et al. 2021, A&A, 649, A26
Lendl, M., Csizmadia, S., Deline, A., et al. 2020, A&A, 643, A94
Lindegren, L., Bastian, U., Biermann, M., et al. 2021, A&A, 649, A4
Linder, E. F., Mordasini, C., Mollière, P., et al. 2019, A&A, 623, A85
Lissauer, J. J., Ragozzine, D., Fabrycky, D. C., et al. 2011, ApJS, 197, 8
Liu, Z., & Ni, D. 2023, A&A, 674, A137
Lodders, K. 2003, ApJ, 591, 1220
Lopez, E. D., & Fortney, J. J. 2014, ApJ, 792, 1
Lopez, T. A., Barros, S. C. C., Santerne, A., et al. 2019, A&A, 631, A90
Loyd, R. O. P., France, K., Youngblood, A., et al. 2016, ApJ, 824, 102
Loyd, R. O. P., France, K., Youngblood, A., et al. 2018, ApJ, 867, 71
Luque, R., & Pallé, E. 2022, Science, 377, 1211
Luque, R., Osborn, H. P., Leleu, A., et al. 2023, Nature, 623, 932
Madhusudhan, N., Sarkar, S., Constantinou, S., et al. 2023, ApJ, 956, L13
Mamajek, E. E. 2009, in American Institute of Physics Conference Series, 1158, Exoplanets and Disks: Their Formation and Diversity, eds. T. Usuda, M. Tamura, & M. Ishii, 3
Marboeuf, U., Thiabaud, A., Alibert, Y., Cabral, N., & Benz, W. 2014, A&A, 570, A36
Marigo, P., Girardi, L., Bressan, A., et al. 2017, ApJ, 835, 77
McKinney, W., et al. 2010, in Proceedings of the 9th Python in Science Conference, 445, Austin, TX, 51
Millholland, S., Wang, S., & Laughlin, G. 2017, ApJ, 849, L33
Mishra, L., Alibert, Y., Udry, S., & Mordasini, C. 2023a, A&A, 670, A68
Mishra, L., Alibert, Y., Udry, S., & Mordasini, C. 2023b, A&A, 670, A69
Mordasini, C. 2020, A&A, 638, A52
Mordasini, C., Alibert, Y., & Benz, W. 2009, A&A, 501, 1139
Mordasini, C., Alibert, Y., Georgy, C., et al. 2012, A&A, 547, A112
Morris, B. M., Delrez, L., Brandeker, A., et al. 2021, A&A, 653, A173
Mousis, O., Marboeuf, U., Lunine, J. I., et al. 2009, ApJ, 696, 1348
Mousis, O., Deleuil, M., Aguichine, A., et al. 2020, ApJ, 896, L22
Mulders, G. D., Pascucci, I., Apai, D., Frasca, A., & Molenda-Żakowicz, J. 2016, AJ, 152, 187
Nair, V., & Hinton, G. E. 2010, in Proceedings of the 27th International Conference on International Conference on Machine Learning, ICML'10 (Madison, WI, USA: Omnipress), 807
Nixon, M. C., & Madhusudhan, N. 2021, MNRAS, 505, 3414
Otegi, J. F., Bouchy, F., & Helled, R. 2020a, A&A, 634, A43
Otegi, J. F., Dorn, C., Helled, R., et al. 2020b, A&A, 640, A135
Owen, J. E., & Campos Estrada, B. 2020, MNRAS, 491, 5287
Owen, J. E., & Wu, Y. 2013, ApJ, 775, 105

Owen, J. E., & Wu, Y. 2017, ApJ, 847, 29
Parmentier, V. & Guillot, T. 2014, A&A, 562, A133
Parmentier, V., Guillot, T., Fortney, J. J., & Marley, M. S. 2015, A&A, 574, A35
Patel, J. A., Egger, J. A., Wilson, T. G., et al. 2023, A&A, 679, A92
Pelletier, S., Benneke, B., Ali-Dib, M., et al. 2023, Nature, 619, 491
Pepe, F., Cristiani, S., Rebolo, R., et al. 2021, A&A, 645, A96
Petigura, E. A., Marcy, G. W., Winn, J. N., et al. 2018, AJ, 155, 89
Pierrehumbert, R. T. 2023, ApJ, 944, 20
Piskunov, N., & Valenti, J. A. 2017, A&A, 597, A16
Ricker, G. R., Winn, J. N., Vanderspek, R., et al. 2015, J. Astron. Telescopes Instrum. Syst., 1, 014003
Rogers, L. A., & Seager, S. 2010, ApJ, 712, 974
Rogers, J. G., Gupta, A., Owen, J. E., & Schlichting, H. E. 2021, MNRAS, 508, 5886
Rogers, J. G., Schlichting, H. E., & Owen, J. E. 2023, ApJ, 947, L19
Salvatier, J., Wiecki, T. V., & Fonnesbeck, C. 2016, PeerJ Comput. Sci., 2, e55
Santos, N. C., Israelian, G., Mayor, M., et al. 2005, A&A, 437, 1127
Schanche, N., Hébrard, G., Collier Cameron, A., et al. 2020, MNRAS, 499, 428
Schib, O., Mordasini, C., & Helled, R. 2022, A&A, 664, A138
Schulik, M., & Booth, R. A. 2023, MNRAS, 523, 286
Seager, S., Kuchner, M., Hier-Majumder, C. A., & Militzer, B. 2007, ApJ, 669, 1279
Selsis, F., Leconte, J., Turbet, M., Chaverot, G., & Bolmont, É. 2023, Nature, 620, 287
Serrano, L. M., Gandolfi, D., Hoyer, S., et al. 2022, A&A, 667, A1
Skrutskie, M. F., Cutri, R. M., Stiening, R., et al. 2006, AJ, 131, 1163
Sotin, C., Grasset, O., & Mocquet, A. 2007, Icarus, 191, 337
Soubiran, F., & Militzer, B. 2015, ApJ, 806, 228
Spada, F., Demarque, P., Kim, Y. C., & Sills, A. 2013, ApJ, 776, 87
Szabó, G. M., Gandolfi, D., Brandeker, A., et al. 2021, A&A, 654, A159
Tanaka, H., Takeuchi, T., & Ward, W. R. 2002, ApJ, 565, 1257
Thiabaud, A., Marboeuf, U., Alibert, Y., et al. 2014, A&A, 562, A27
Thiabaud, A., Marboeuf, U., Alibert, Y., Leya, I., & Mezger, K. 2015, A&A, 574, A138
Turbet, M., Ehrenreich, D., Lovis, C., Bolmont, E., & Fauchez, T. 2019, A&A, 628, A12
Turbet, M., Bolmont, E., Ehrenreich, D., et al. 2020, A&A, 638, A41
Tychoniec, Ł., Tobin, J. J., Karska, A., et al. 2018, ApJS, 238, 19
Ulmer-Moll, S., Osborn, H. P., Tuson, A., et al. 2023, A&A, 674, A43
Unterborn, C. T., Desch, S. J., Haldemann, J., et al. 2023, ApJ, 944, 42
Valencia, D., Guillot, T., Parmentier, V., & Freedman, R. S. 2013, ApJ, 775, 10
Valenti, J. A., & Piskunov, N. 1996, A&AS, 118, 595
Vazan, A., Sari, R., & Kessel, R. 2022, ApJ, 926, 150
Venturini, J., Guilera, O. M., Haldemann, J., Ronco, M. P., & Mordasini, C. 2020a, A&A, 643, L1
Venturini, J., Guilera, O. M., Ronco, M. P., & Mordasini, C. 2020b, A&A, 644, A174
Venturini, J., Ronco, M. P., Guilera, O. M., et al. 2024, A&A, 686, A9
Virtanen, P., Gommers, R., Oliphant, T. E., et al. 2020, Nature Methods, 17, 261
Vissapragada, S., Jontof-Hutter, D., Shporer, A., et al. 2020, AJ, 159, 108
Voelkel, O., Klahr, H., Mordasini, C., Emsenhuber, A., & Lenz, C. 2020, A&A, 642, A75
Voelkel, O., Deienno, R., Kretke, K., & Klahr, H. 2021, A&A, 645, A131
Waskom, M. L. 2021, J. Open Source Softw., 6, 3021
Weder, J., Mordasini, C., & Emsenhuber, A. 2023, A&A, 674, A165
Weiss, L. M., Marcy, G. W., Petigura, E. A., et al. 2018, AJ, 155, 48
Wilson, T. G., Goffo, E., Alibert, Y., et al. 2022, MNRAS, 511, 1043
Wright, E. L., Eisenhardt, P. R. M., Mainzer, A. K., et al. 2010, AJ, 140, 1868
Youngblood, A., France, K., Loyd, R. O. P., et al. 2016, ApJ, 824, 101
Youngblood, A., France, K., Loyd, R. O. P., et al. 2017, ApJ, 843, 31
Zeng, L., Jacobsen, S. B., Sasselov, D. D., et al. 2019, PNAS, 116, 9723

[1] Weltraumforschung und Planetologie, Physikalisches Institut, University of Bern, Gesellschaftsstrasse 6, 3012 Bern, Switzerland
e-mail: jo-ann.egger@unibe.ch
[2] Center for Space and Habitability, University of Bern, Gesellschaftsstrasse 6, 3012 Bern, Switzerland
[3] Department of Physics and Kavli Institute for Astrophysics and Space Research, Massachusetts Institute of Technology, Cambridge, MA 02139, USA
[4] Space Research Institute, Austrian Academy of Sciences, Schmiedlstrasse 6, 8042 Graz, Austria
[5] European Space Agency (ESA), European Space Research and Technology Centre (ESTEC), Keplerlaan 1, 2201 AZ Noordwijk, The Netherlands
[6] Observatoire astronomique de l'Université de Genève, Chemin Pegasi 51, 1290 Versoix, Switzerland
[7] Department of Astronomy, Stockholm University, AlbaNova University Center, 10691 Stockholm, Sweden
[8] INAF – Osservatorio Astrofisico di Torino, Via Osservatorio 20, 10025 Pino Torinese, Italy
[9] Department of Physics, University of Warwick, Gibbet Hill Road, Coventry CV4 7AL, UK
[10] Instituto de Astrofisica e Ciencias do Espaco, Universidade do Porto, CAUP, Rua das Estrelas, 4150-762 Porto, Portugal
[11] Astrobiology Research Unit, Université de Liège, Allée du 6 Août 19C, 4000 Liège, Belgium
[12] Space sciences, Technologies and Astrophysics Research (STAR) Institute, Université de Liège, Allée du 6 Août 19C, 4000 Liège, Belgium
[13] Institute of Astronomy, KU Leuven, Celestijnenlaan 200D, 3001 Leuven, Belgium
[14] Cavendish Laboratory, JJ Thomson Avenue, Cambridge CB3 0HE, UK
[15] Dipartimento di Fisica e Astronomia "Galileo Galilei", Università degli Studi di Padova, Vicolo dell'Osservatorio 3, 35122 Padova, Italy
[16] INAF, Osservatorio Astronomico di Padova, Vicolo dell'Osservatorio 5, 35122 Padova, Italy
[17] Department of Astronomy & Astrophysics, University of Chicago, Chicago, IL 60637, USA
[18] Instituto de Astrofísica de Canarias, Vía Láctea s/n, 38200 La Laguna, Tenerife, Spain
[19] Departamento de Astrofísica, Universidad de La Laguna, Astrofísico Francisco Sanchez s/n, 38206 La Laguna, Tenerife, Spain
[20] Admatis, 5. Kandó Kálmán Street, 3534 Miskolc, Hungary
[21] Depto. de Astrofísica, Centro de Astrobiología (CSIC-INTA), ESAC campus, 28692 Villanueva de la Cañada (Madrid), Spain
[22] Departamento de Fisica e Astronomia, Faculdade de Ciencias, Universidade do Porto, Rua do Campo Alegre, 4169-007 Porto, Portugal
[23] Institute of Optical Sensor Systems, German Aerospace Center (DLR), Rutherfordstrasse 2, 12489 Berlin, Germany
[24] Centre for Exoplanet Science, SUPA School of Physics and Astronomy, University of St Andrews, North Haugh, St Andrews KY16 9SS, UK
[25] CFisUC, Department of Physics, University of Coimbra, 3004-516 Coimbra, Portugal
[26] AIRBUS DS Madrid, Paseo John Lennon 2, 28906 Getafe (Madrid), Spain
[27] Institute of Planetary Research, German Aerospace Center (DLR), Rutherfordstrasse 2, 12489 Berlin, Germany
[28] INAF, Osservatorio Astrofisico di Torino, Via Osservatorio, 20, 10025 Pino Torinese To, Italy
[29] Centre for Mathematical Sciences, Lund University, Box 118, 221 00 Lund, Sweden
[30] Aix Marseille Univ, CNRS, CNES, LAM, 38 rue Frédéric Joliot-Curie, 13388 Marseille, France
[31] ELTE Gothard Astrophysical Observatory, Szent Imre h. u. 112, 9700 Szombathely, Hungary
[32] SRON Netherlands Institute for Space Research, Niels Bohrweg 4, 2333 CA Leiden, The Netherlands
[33] Centre Vie dans l'Univers, Faculté des sciences, Université de Genève, Quai Ernest-Ansermet 30, 1211 Genève 4, Switzerland
[34] Leiden Observatory, University of Leiden, PO Box 9513, 2300 RA Leiden, The Netherlands
[35] Department of Space, Earth and Environment, Chalmers University of Technology, Onsala Space Observatory, 439 92 Onsala, Sweden
[36] Dipartimento di Fisica, Università degli Studi di Torino, via Pietro Giuria 1, 10125, Torino, Italy
[37] National and Kapodistrian University of Athens, Department of Physics, University Campus, Zografos 157 84, Athens, Greece
[38] Department of Astrophysics, University of Vienna, Türkenschanzstrasse 17, 1180 Vienna, Austria
[39] Institute for Theoretical Physics and Computational Physics, Graz University of Technology, Petersgasse 16, 8010 Graz, Austria

[40] Konkoly Observatory, Research Centre for Astronomy and Earth Sciences, Konkoly Thege Miklós út 15-17, 1121 Budapest, Hungary

[41] ELTE Eötvös Loránd University, Institute of Physics, Pázmány Péter sétány 1/A, 1117 Budapest, Hungary

[42] Lund Observatory, Division of Astrophysics, Department of Physics, Lund University, Box 118, 22100 Lund, Sweden

[43] IMCCE, UMR8028 CNRS, Observatoire de Paris, PSL Univ., Sorbonne Univ., 77 av. Denfert-Rochereau, 75014 Paris, France

[44] Institut d'astrophysique de Paris, UMR7095 CNRS, Université Pierre & Marie Curie, 98bis blvd. Arago, 75014 Paris, France

[45] Astrophysics Group, Lennard Jones Building, Keele University, Staffordshire, ST5 5BG, UK

[46] European Space Agency, ESA - European Space Astronomy Centre, Camino Bajo del Castillo s/n, 28692 Villanueva de la Cañada, Madrid, Spain

[47] INAF, Osservatorio Astrofisico di Catania, Via S. Sofia 78, 95123 Catania, Italy

[48] ETH Zurich, Department of Physics, Wolfgang-Pauli-Strasse 2, 8093 Zurich, Switzerland

[49] Institut fuer Geologische Wissenschaften, Freie Universitaet Berlin, Maltheserstrasse 74-100, 12249 Berlin, Germany

[50] Institut de Ciencies de l'Espai (ICE, CSIC), Campus UAB, Can Magrans s/n, 08193 Bellaterra, Spain

[51] Institut d'Estudis Espacials de Catalunya (IEEC), 08860 Castelldefels (Barcelona), Spain

[52] Instituto de Astrofísica e Ciências do Espaço, Universidade do Porto, CAUP, Rua das Estrelas, 4150-762 Porto, Portugal

[53] Departamento de Física e Astronomia, Faculdade de Ciências, Universidade do Porto, Rua do Campo Alegre, 4169-007 Porto, Portugal

[54] HUN-REN-ELTE Exoplanet Research Group, Szent Imre h. u. 112., Szombathely 9700, Hungary

[55] Institute of Astronomy, University of Cambridge, Madingley Road, Cambridge, CB3 0HA, UK

# Appendix A: Observations and data analysis
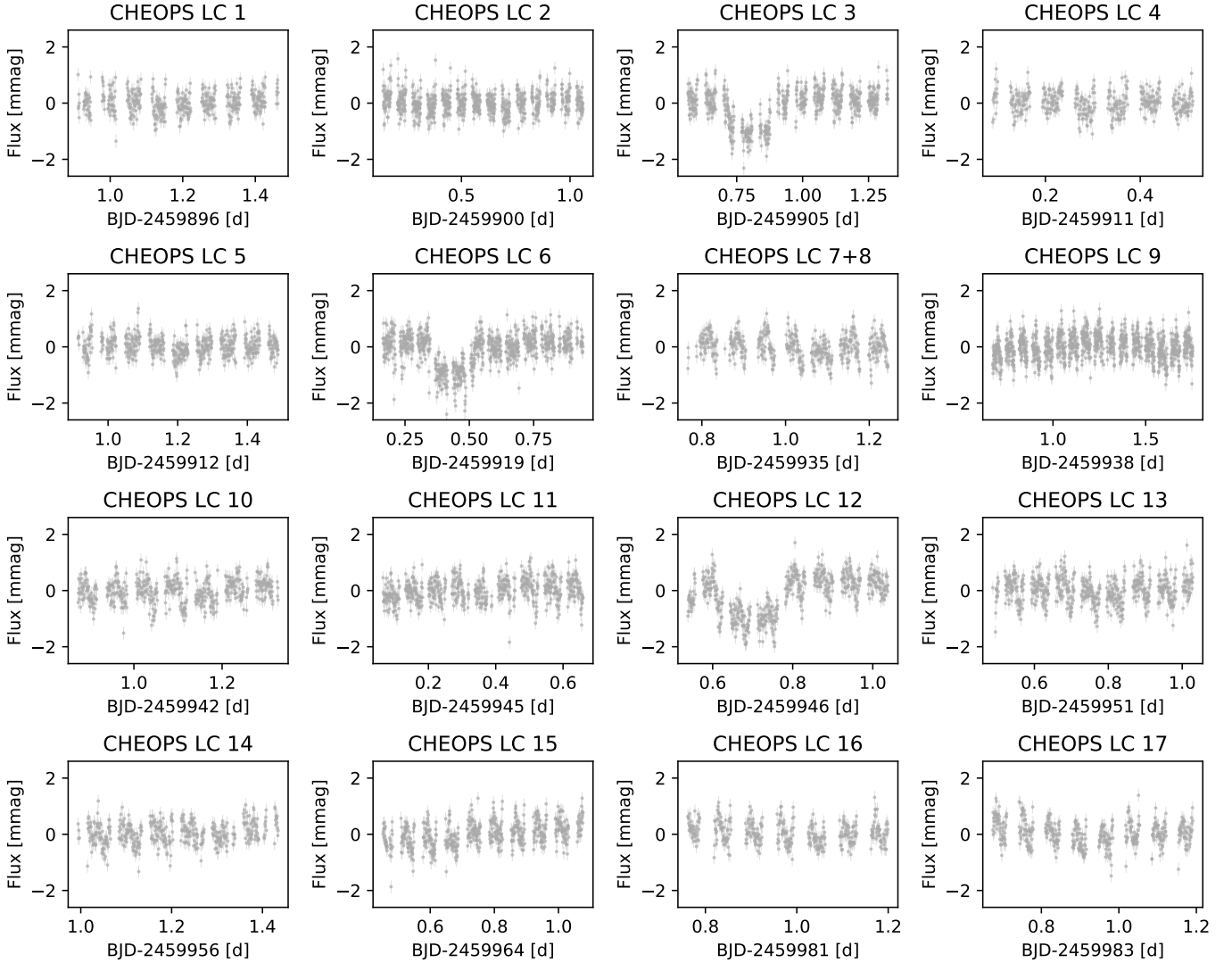


**Fig. A.1.** Undetrended CHEOPS light curves of HIP 29442, identified by the IDs introduced in Table 2.

# Appendix B: Internal structure analysis

## B.1. Chosen DNN architectures

**Table B.1.** Network architectures of the best-performing DNNs used as a forward model in the `plaNETic` code.

| Model | | HL1 | HL2 | HL3 | HL4 | HL5 | HL6 |
|---|---|---|---|---|---|---|---|
| PREV | | 2048 | 2048 | 2048 | 2048 | 2048 | 2048 |
| A | M1 | 2048 | 2048 | 2048 | 2048 | 2048 | 2048 |
| A | M2 | 2048 | 2048 | 2048 | 2048 | 2048 | 2048 |
| B | M1 | 512 | 1024 | 2048 | 1024 | 512 | 256 |
| B | M2 | 2048 | 2048 | 2048 | 2048 | 2048 | 2048 |

**Notes.** Network architectures are specified for both the old version of `plaNETic` (denoted as PREV) and the version that is newly introduced in this work. For the new version, separate DNNs were trained for different planetary mass ranges (M1 for planets from 0.5 to 6 $M_\oplus$, M2 for planets from 6 to 15 $M_\oplus$) and water prior options (A assuming a formation outside the iceline, B inside). The table shows the number of units in each of the hidden layers (HL) of the DNN in question.

## B.2. DNN performance analysis

**Table B.2.** Time needed to calculate the transit radii of 100 randomly sampled planetary structures from the posteriors of the internal structure models for HIP 29442 b, c, and d, both with the trained DNNs and the full planetary structure model from BICEPS.

| Model | HIP 29442 b | | | HIP 29442 c | | | HIP 29442 d | | |
|---|---|---|---|---|---|---|---|---|---|
| | $t_{BICEPS}$ [s] | $t_{DNN}$ [s] | Speed-up | $t_{BICEPS}$ [s] | $t_{DNN}$ [s] | Speed-up | $t_{BICEPS}$ [s] | $t_{DNN}$ [s] | Speed-up |
| A1 | 1363 | 0.034 | 40088× | 1462 | 0.038 | 38474× | 1454 | 0.034 | 42706× |
| A2 | 1209 | 0.031 | 39000× | 1415 | 0.036 | 39306× | 1402 | 0.036 | 38944× |
| A3 | 1350 | 0.032 | 42188× | 1372 | 0.035 | 39200× | 1341 | 0.035 | 38314× |
| B1 | 2414 | 0.036 | 67056× | 2405 | 0.035 | 68714× | 2403 | 0.038 | 63237× |
| B2 | 2070 | 0.035 | 59143× | 2085 | 0.036 | 57917× | 2079 | 0.038 | 54711× |
| B3 | 2329 | 0.036 | 64694× | 2295 | 0.035 | 65571× | 2295 | 0.034 | 67500× |

## B.3. Internal structure modelling posteriors

**Table B.3.** Median and one-sigma errors for the posterior distributions of the internal structure modelling for HIP 29442 b using the new version of `plaNETic` described in Section 4.2.

| Water prior | Formation outside iceline (water-rich) | | | Formation inside iceline (water-poor) | | |
|---|---|---|---|---|---|---|
| Si/Mg/Fe prior | Stellar (A1) | Iron-enriched (A2) | Free (A3) | Stellar (B1) | Iron-enriched (B2) | Free (B3) |
| $w_{core}$ [%] | $11.8^{+9.2}_{-8.1}$ | $16.0^{+15.2}_{-11.2}$ | $13.1^{+16.0}_{-9.5}$ | $17.6^{+11.8}_{-11.5}$ | $22.2^{+19.2}_{-15.4}$ | $17.6^{+20.8}_{-12.7}$ |
| $w_{mantle}$ [%] | $58.4^{+16.2}_{-14.8}$ | $51.4^{+19.1}_{-15.6}$ | $54.4^{+19.4}_{-16.8}$ | $76.6^{+11.5}_{-11.9}$ | $71.6^{+15.5}_{-19.5}$ | $76.5^{+13.1}_{-21.3}$ |
| $w_{envelope}$ [%] | $28.3^{+17.5}_{-17.0}$ | $29.2^{+17.2}_{-17.1}$ | $28.5^{+17.4}_{-17.0}$ | $5.9^{+0.3}_{-0.3}$ | $6.3^{+0.5}_{-0.7}$ | $6.0^{+0.9}_{-0.9}$ |
| $Z_{envelope}$ [%] | $65.0^{+10.5}_{-25.6}$ | $64.7^{+10.7}_{-26.1}$ | $65.6^{+10.5}_{-25.7}$ | $0.5^{+0.3}_{-0.2}$ | $0.5^{+0.2}_{-0.2}$ | $0.5^{+0.2}_{-0.2}$ |
| $x_{Fe,core}$ [%] | $90.4^{+6.5}_{-6.4}$ | $90.4^{+6.5}_{-6.4}$ | $90.5^{+6.5}_{-6.5}$ | $90.2^{+7.0}_{-6.1}$ | $90.4^{+6.5}_{-6.4}$ | $90.4^{+6.5}_{-6.4}$ |
| $x_{S,core}$ [%] | $9.6^{+6.4}_{-6.5}$ | $9.6^{+6.4}_{-6.5}$ | $9.5^{+6.5}_{-6.5}$ | $9.8^{+6.1}_{-7.0}$ | $9.6^{+6.4}_{-6.5}$ | $9.6^{+6.4}_{-6.5}$ |
| $x_{Si,mantle}$ [%] | $36.7^{+6.5}_{-5.7}$ | $32.7^{+9.2}_{-8.8}$ | $33.0^{+29.6}_{-23.0}$ | $35.5^{+7.2}_{-6.5}$ | $32.7^{+9.2}_{-8.8}$ | $33.6^{+29.5}_{-23.3}$ |
| $x_{Mg,mantle}$ [%] | $44.9^{+7.5}_{-6.4}$ | $38.5^{+10.6}_{-10.3}$ | $36.3^{+30.6}_{-24.4}$ | $45.1^{+8.1}_{-7.4}$ | $38.6^{+10.6}_{-10.3}$ | $36.1^{+30.1}_{-24.5}$ |
| $x_{Fe,mantle}$ [%] | $18.4^{+9.2}_{-11.7}$ | $28.0^{+18.5}_{-18.4}$ | $22.0^{+24.2}_{-16.1}$ | $19.5^{+9.4}_{-12.7}$ | $28.0^{+18.6}_{-18.4}$ | $21.7^{+24.0}_{-15.7}$ |

**Table B.4.** Median and one-sigma errors for the posterior distributions of the internal structure modelling for HIP 29442 c using the new version of `plaNETic` described in Section 4.2.

| Water prior | Formation outside iceline (water-rich) | | | Formation inside iceline (water-poor) | | |
|---|---|---|---|---|---|---|
| Si/Mg/Fe prior | Stellar (A1) | Iron-enriched (A2) | Free (A3) | Stellar (B1) | Iron-enriched (B2) | Free (B3) |
| $w_{core}$ [%] | $18.7^{+11.1}_{-12.3}$ | $29.2^{+19.8}_{-19.5}$ | $31.4^{+21.5}_{-21.2}$ | $20.4^{+10.6}_{-12.9}$ | $35.4^{+19.1}_{-22.5}$ | $39.2^{+20.9}_{-25.6}$ |
| $w_{mantle}$ [%] | $80.3^{+12.5}_{-11.2}$ | $68.2^{+19.5}_{-20.3}$ | $65.4^{+21.3}_{-22.2}$ | $75.4^{+14.3}_{-10.9}$ | $64.6^{+22.5}_{-19.1}$ | $60.7^{+25.6}_{-20.9}$ |
| $w_{envelope}$ [%] | $0.6^{+1.2}_{-0.4}$ | $2.3^{+2.5}_{-1.5}$ | $2.9^{+3.1}_{-2.0}$ | $\left(1.3^{+0.3}_{-0.2}\right) 10^{-4}$ | $\left(1.7^{+1.5}_{-0.5}\right) 10^{-4}$ | $\left(2.1^{+2.8}_{-0.9}\right) 10^{-4}$ |
| $Z_{envelope}$ [%] | $99.8^{+0.2}_{-1.3}$ | $99.9^{+0.1}_{-1.4}$ | $99.9^{+0.1}_{-1.4}$ | $0.5^{+0.3}_{-0.2}$ | $0.5^{+0.2}_{-0.2}$ | $0.5^{+0.2}_{-0.2}$ |
| $x_{Fe,core}$ [%] | $90.3^{+6.7}_{-6.3}$ | $90.6^{+6.4}_{-6.6}$ | $90.5^{+6.4}_{-6.5}$ | $90.0^{+6.9}_{-6.6}$ | $90.3^{+6.5}_{-6.4}$ | $90.4^{+6.5}_{-6.4}$ |
| $x_{S,core}$ [%] | $9.7^{+6.3}_{-6.7}$ | $9.4^{+6.6}_{-6.4}$ | $9.5^{+6.5}_{-6.4}$ | $10.0^{+6.6}_{-6.9}$ | $9.7^{+6.4}_{-6.5}$ | $9.6^{+6.4}_{-6.5}$ |
| $x_{Si,mantle}$ [%] | $37.1^{+6.8}_{-5.8}$ | $29.7^{+10.5}_{-8.0}$ | $22.5^{+25.4}_{-15.7}$ | $36.4^{+6.3}_{-6.3}$ | $28.8^{+10.4}_{-8.0}$ | $20.0^{+22.9}_{-14.2}$ |
| $x_{Mg,mantle}$ [%] | $45.6^{+7.1}_{-6.4}$ | $35.1^{+11.9}_{-9.6}$ | $33.8^{+23.2}_{-19.7}$ | $45.9^{+8.5}_{-7.2}$ | $34.0^{+12.1}_{-9.5}$ | $33.9^{+24.6}_{-18.7}$ |
| $x_{Fe,mantle}$ [%] | $16.8^{+9.9}_{-10.9}$ | $35.0^{+16.9}_{-21.9}$ | $38.8^{+20.2}_{-24.2}$ | $16.8^{+10.9}_{-9.8}$ | $36.8^{+17.0}_{-21.9}$ | $40.7^{+20.1}_{-25.4}$ |

**Table B.5.** Median and one-sigma errors for the posterior distributions of the internal structure modelling for HIP 29442 d using the new version of `plaNETic` described in Section 4.2.

| Water prior | Formation outside iceline (water-rich) | | | Formation inside iceline (water-poor) | | |
|---|---|---|---|---|---|---|
| Si/Mg/Fe prior | Stellar (A1) | Iron-enriched (A2) | Free (A3) | Stellar (B1) | Iron-enriched (B2) | Free (B3) |
| $w_{core}$ [%] | $18.7^{+11.0}_{-12.2}$ | $31.4^{+19.9}_{-20.9}$ | $33.9^{+22.0}_{-22.8}$ | $21.9^{+10.6}_{-12.5}$ | $37.4^{+18.5}_{-23.4}$ | $41.3^{+20.7}_{-26.6}$ |
| $w_{mantle}$ [%] | $80.6^{+12.3}_{-11.2}$ | $66.7^{+20.9}_{-20.1}$ | $63.5^{+22.8}_{-22.5}$ | $78.1^{+12.5}_{-10.6}$ | $62.6^{+23.4}_{-18.5}$ | $58.7^{+26.6}_{-20.7}$ |
| $w_{envelope}$ [%] | $0.5^{+0.9}_{-0.3}$ | $1.6^{+2.1}_{-1.1}$ | $2.1^{+2.7}_{-1.5}$ | $\left(1.2^{+0.5}_{-0.2}\right) 10^{-4}$ | $\left(1.8^{+2.1}_{-0.6}\right) 10^{-4}$ | $\left(2.3^{+4.2}_{-1.1}\right) 10^{-4}$ |
| $Z_{envelope}$ [%] | $99.8^{+0.2}_{-1.3}$ | $99.8^{+0.2}_{-1.5}$ | $99.8^{+0.1}_{-1.5}$ | $0.5^{+0.2}_{-0.3}$ | $0.5^{+0.2}_{-0.3}$ | $0.5^{+0.2}_{-0.2}$ |
| $x_{Fe,core}$ [%] | $90.4^{+6.5}_{-6.4}$ | $90.6^{+6.4}_{-6.5}$ | $90.5^{+6.5}_{-6.5}$ | $89.1^{+6.7}_{-5.5}$ | $90.4^{+6.4}_{-6.3}$ | $90.4^{+6.4}_{-6.4}$ |
| $x_{S,core}$ [%] | $9.6^{+6.4}_{-6.5}$ | $9.4^{+6.5}_{-6.4}$ | $9.5^{+6.5}_{-6.5}$ | $10.9^{+5.5}_{-6.7}$ | $9.6^{+6.3}_{-6.4}$ | $9.6^{+6.4}_{-6.4}$ |
| $x_{Si,mantle}$ [%] | $37.0^{+7.0}_{-5.7}$ | $29.1^{+10.7}_{-8.0}$ | $20.2^{+23.6}_{-14.3}$ | $36.6^{+7.3}_{-6.7}$ | $28.9^{+10.5}_{-8.3}$ | $18.5^{+22.2}_{-13.4}$ |
| $x_{Mg,mantle}$ [%] | $45.5^{+7.0}_{-6.2}$ | $34.4^{+12.2}_{-9.6}$ | $33.9^{+22.5}_{-18.8}$ | $46.5^{+7.8}_{-7.4}$ | $34.1^{+12.2}_{-9.7}$ | $34.5^{+24.6}_{-18.4}$ |
| $x_{Fe,mantle}$ [%] | $16.9^{+9.7}_{-10.7}$ | $36.3^{+16.9}_{-22.7}$ | $41.7^{+18.9}_{-25.8}$ | $16.2^{+10.4}_{-9.9}$ | $36.6^{+17.6}_{-22.1}$ | $41.7^{+19.8}_{-26.0}$ |

**Table B.6.** Median and one-sigma errors for the posterior distributions of the internal structure modelling for HIP 29442 b, c, and d using the previous version of our internal structure model described in Section 4.1.

| | HIP 29442 b | HIP 29442 c | HIP 29442 d |
|---|---|---|---|
| $w_{core}$ [%] | $13.8^{+8.22}_{-8.11}$ | $17.7^{+9.5}_{-10.3}$ | $17.9^{+9.6}_{-10.3}$ |
| $w_{mantle}$ [%] | $59.4^{+14.3}_{-13.4}$ | $75.5^{+10.9}_{-9.4}$ | $78.3^{+10.6}_{-9.7}$ |
| $w_{water}$ [%] | $22.4^{+17.3}_{-15.6}$ | $5.7^{+5.6}_{-3.8}$ | $2.9^{+3.8}_{-2.1}$ |
| $w_{H/He}$ [%] | $3.0^{+0.8}_{-0.6}$ | $\left(1.7^{+10.7}_{-1.5}\right) 10^{-7}$ | $\left(1.3^{+7.0}_{-1.1}\right) 10^{-7}$ |
| $x_{Fe,core}$ [%] | $90.3^{+6.6}_{-6.3}$ | $90.3^{+6.5}_{-6.4}$ | $90.4^{+6.5}_{-6.4}$ |
| $x_{S,core}$ [%] | $9.7^{+6.3}_{-6.6}$ | $9.7^{+6.4}_{-6.5}$ | $9.6^{+6.4}_{-6.5}$ |
| $x_{Si,mantle}$ [%] | $39.4^{+5.3}_{-4.0}$ | $39.2^{+5.2}_{-3.9}$ | $39.0^{+5.1}_{-3.8}$ |
| $x_{Mg,mantle}$ [%] | $44.9^{+7.3}_{-6.9}$ | $44.7^{+7.2}_{-6.7}$ | $44.5^{+7.3}_{-6.6}$ |
| $x_{Fe,mantle}$ [%] | $15.0^{+9.3}_{-9.6}$ | $15.5^{+9.0}_{-9.6}$ | $15.9^{+8.6}_{-9.5}$ |

**Notes.** Note that all mass fractions are in relation to the total planet mass, including also the H/He envelope, to be more comparable to the results generated with the new version of `plaNETic`. However, this means that these results are not comparable with the ones reported in our own previous work where we employed the same model.